NUCLEAR DATA AND MEASUREMENTS SERIES

ANL/NDM-120

Fast-Neutron Total and Scattering Cross Sections of ^{58}Ni and Nuclear Models

by

A.B. Smith, P.T. Guenther, J.F. Whalen, and S. Chiba

July 1991

ARGONNE NATIONAL LABORATORY,
ARGONNE, ILLINOIS 60439, U.S.A.

NUCLEAR DATA AND MEASUREMENTS SERIES

ANL/NDM-120

FAST-NEUTRON TOTAL AND SCATTERING CROSS SECTIONS OF ^{58}Ni AND NUCLEAR MODELS

A. B. Smith, P. T. Guenther, J. F. Whalen, and S. Chiba

July 1991

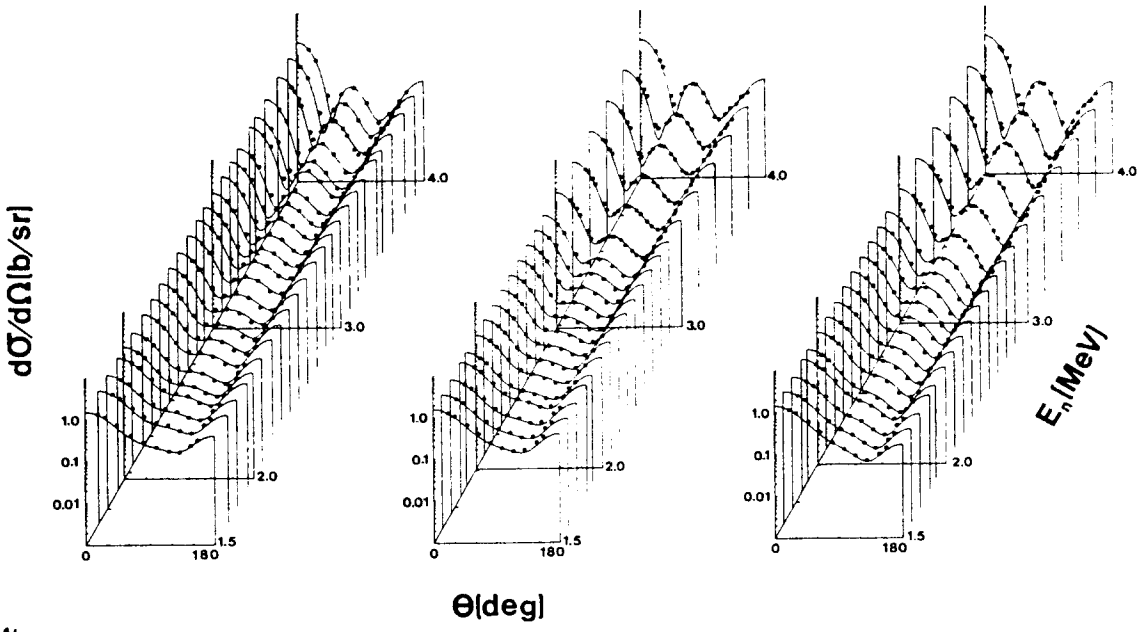

ARGONNE NATIONAL LABORATORY, ARGONNE, ILLINOIS

Operated by THE UNIVERSITY OF CHICAGO

for the U. S. DEPARTMENT OF ENERGY

under Contract W-31-109-Eng-38

Reproduced from the best available copy.

Available to DOE and DOE contractors from the
Office of Scientific and Technical Information
P.O. Box 62
Oak Ridge, TN 37831
Prices available from (615) 576-8401, FTS 626-8401

Available to the public from the
National Technical Information Service
U.S. Department of Commerce
5285 Port Royal Road
Springfield, VA 22161

ANL/NDM-120

FAST-NEUTRON TOTAL AND SCATTERING CROSS SECTIONS OF ^{58}Ni AND NUCLEAR MODELS

by

A. B. Smith, P. T. Guenther, J. F. Whalen, and S. Chiba*

July 1991

Keywords:

Measured σ_t, $d\sigma/d\Omega_{el}$ and $d\sigma/d\Omega_{inel}$ for 1-10 MeV neutrons. Optical-Statistical, dispersive-optical and coupled-channels models. Physical interpretation.

Engineering Physics Division
Argonne National Laboratory
9700 South Cass Avenue
Argonne, Illinois 60439
U. S. A.

* Visiting scientist from Japan Atomic Energy Research Institute, Tokai Establishment.

NUCLEAR DATA AND MEASUREMENTS SERIES

The Nuclear Data and Measurements Series presents results of studies in the field of microscopic nuclear data. The primary objective is the dissemination of information in the comprehensive form required for nuclear technology applications. This Series is devoted to: a) measured microscopic nuclear parameters, b) experimental techniques and facilities employed in measurements, c) the analysis, correlation and interpretation of nuclear data, and d) the evaluation of nuclear data. Contributions to this Series are reviewed to assure technical competence and, unless otherwise stated, the contents can be formally referenced. This Series does not supplant formal journal publication, but it does provide the more extensive information required for technological applications (e.g., tabulated numerical data) in a timely manner.

TABLE OF CONTENTS

INFORMATION ABOUT OTHER ISSUES OF THE ANL/NDM SERIES

A list of titles and authors for all the previous issues appears in reports of the series. The list for reports ANL/NDM-1 through ANL/NDM-75 appears in ANL/NDM-76, and ANL/NDM-91 contains the list for reports ANL/NDM-76 through ANL/NDM-90. Below is the list for ANL/NDM-91 up to the current report. Requests for a complete list of titles, or for copies of previous reports, should be directed to:

Section Secretary
Applied Nuclear Physics Section
Engineering Physics Division
Building 316
Argonne National Laboratory
9700 South Cass Avenue
Argonne, Illinois 60439
U.S.A.

ANL/NDM-91 A.B. Smith, P.T. Guenther and R.D. Lawson, *On the Energy Dependence of the Optical Model of Neutron Scattering from Niobium*, May 1985.

ANL/NDM-92 Donald L. Smith, *Nuclear Data Uncertainties (Vol.-I): Basic Concepts of Probability*, December 1988.

ANL/NDM-93 D.L. Smith, J.W. Meadows and M.M. Bretscher, *Integral Cross-section Measurements for $^{7}Li(n,n't)^{4}He$, $^{27}Al(n,p)^{27}Mg$, $^{27}Al(n,a)^{24}Na$, $^{58}Ni(n,p)^{58}Co$, and $^{60}Ni(n,p)^{60}Co$ Relative to ^{238}U Neutron Fission in the Thick-target $^{9}Be(d,n)^{10}B$ Spectrum at E_d = 7 MeV*, October 1985.

ANL/NDM-94 A.B. Smith, D.L. Smith, P. Rousset, R.D. Lawson and R.J. Howerton, *Evaluated Neutronic Data File for Yttrium*, January 1986.

ANL/NDM-95 Donald L. Smith and James W. Meadows, *A Facility for High-intensity Neutron Irradiations Using Thick-target Sources at the Argonne Fast-neutron Generator*, May 1986.

ANL/NDM-96 M. Sugimoto, A.B. Smith and P.T. Guenther, *Ratio of the Prompt-fission-neutron Spectrum of Plutonium-239 to that of Uranium-235*, September 1986.

ANL/NDM-97 J.W. Meadows, *The Fission Cross Sections of ^{230}Th, ^{232}Th, ^{233}U, ^{234}U, ^{236}U, ^{238}U, ^{237}Np, ^{239}Pu, and ^{242}Pu Relative ^{235}U at 14.74 MeV Neutron Energy*, December 1986.

ANL/NDM-98 J.W. Meadows, *The Fission Cross Section Ratios and Error Analysis for Ten Thorium, Uranium, Neptunium and Plutonium Isotopes at 14.74-MeV Neutron Energy*, March 1987.

ANL/NDM-99 Donald L. Smith, *Some Comments on the Effects of Long-range Correlations in Covariance Matrices for Nuclear Data*, March 1987.

ANL/NDM-100 A.B. Smith, P.T. Guenther and R.D. Lawson, *The Energy Dependence of the Optical-model Potential for Fast-neutron Scattering from Bismuth*, May 1987.

ANL/NDM-101 A.B. Smith, P.T. Guenther, J.F. Whalen and R.D. Lawson, *Cobalt: Fast Neutrons and Physical Models*, July 1987.

ANL/NDM-102 D. L Smith, *Investigation of the Influence of the Neutron Spectrum in Determinations of Integral Neutron Cross-Section Ratios*, November 1987.

ANL/NDM-103 A.B. Smith, P.T. Guenther and B. Micklich, *Spectrum of Neutrons Emitted From a Thick Beryllium Target Bombarded With 7 MeV Deuterons*, January 1988.

ANL/NDM-104 L.P. Geraldo and D.L. Smith, *Some Thoughts on Positive Definiteness in the Consideration of Nuclear Data Covariance Matrices*, January 1988.

ANL/NDM-105 A.B. Smith, D.L. Smith, P.T. Guenther, J.W. Meadows, R.D. Lawson, R.J. Howerton, and T. Djemil, *Neutronic Evaluated Nuclear-Data File for Vanadium*, May 1988.

ANL/NDM-106 A.B. Smith, P.T. Guenther, and R.D. Lawson, *Fast-Neutron Elastic Scattering from Elemental Vanadium*, March 1988.

ANL/NDM-107 P. Guenther, R. Lawson, J. Meadows, M. Sugimoto, A. Smith, D. Smith, and R. Howerton, *An Evaluated Neutronic Data File for Elemental Cobalt*, August 1988.

ANL/NDM-108 M. Sugimoto, P.T. Guenther, J.E. Lynn, A.B. Smith, and J.F. Whalen, *Some Comments on the Interaction of Fast-Neutrons with Beryllium*, November 1988.

ANL/NDM-109 P.T. Guenther, R.D. Lawson, J.W. Meadows, A.B. Smith, D.L. Smith, and M. Sugimoto, *An Evaluated Neutronic Data File for Bismuth*, November 1989.

ANL/NDM-110 D.L. Smith and L.P. Geraldo, *A Vector Model for Error Propagation*, March 1989.

ANL/NDM-111 J.E. Lynn, *Fifty Years of Nuclear Fission*, June 1989.

ANL/NDM-112 S. Chiba, P.T. Guenther, and A.B. Smith, *Some Remarks on the Neutron Elastic- and Inelastic-Scattering Cross Sections of Palladium*, May 1989.

ANL/NDM-113 J.E. Lynn, *Resonance Effects in Neutron Scattering Lengths*, June 1989.

ANL/NDM-114 A.B. Smith, R.D. Lawson, and P.T. Guenther, *Ambiguities in the Elastic Scattering of 8 MeV Neutrons from Adjacent Nuclei*, October 1989.

ANL/NDM-115 A.B. Smith, S. Chiba, D.L. Smith, J.W. Meadows, P.T. Guenther, R.D. Lawson, and R.J. Howerton, *Evaluated Neutronic File for Indium*, January 1990.

ANL/NDM-116 S. Chiba, P.T. Guenther, R.D. Lawson, and A.B. Smith, *Neutron Scattering from Elemental Indium, the Optical Model, and the Bound-State Potential*, June 1990.

ANL/NDM-117 Donald L. Smith and Luiz P. Geraldo, *An Evaluation of the Nb-93(n,n')Nb-93m Dosimeter Reaction for ENDF/B-VI*, November 1990.

ANL/NDM-118 J. W. Meadows, *Characteristics of the Samples in the FNG Fission Deposit Collection*, December 1990.

ANL/NDM-119 S. Chiba, P. T. Guenther, A. B. Smith and R. D. Lawson, *Fast-Neutron Interaction with Elemental Zirconium and the Dispersive Optical Model*, April 1991.

FAST-NEUTRON TOTAL AND SCATTERING CROSS SECTIONS OF ^{58}Ni AND NUCLEAR MODELS

by

A. B. Smith, P. T. Guenther, J. F. Whalen, and S. Chiba*

ABSTRACT

The neutron total cross sections of ^{58}Ni were measured from ≈ 1 to > 10 MeV using white-source techniques. Differential neutron elastic-scattering cross sections were measured from ≈ 4.5 to 10 MeV at ≈ 0.5 MeV intervals with ≥ 75 differential values per distribution. Differential neutron inelastic-scattering cross sections were measured, corresponding to fourteen levels with excitations up to 4.8 MeV. The measured results, combined with relevant values available in the literature, were interpreted in terms of optical-statistical and coupled-channels models using both vibrational and rotational coupling schemes. The physical implications of the experimental results and their interpretation are discussed in the contexts of optical-statistical, dispersive-optical, and coupled-channels models.

* Visiting scientist from Japan Atomic Energy Research Institute, Tokai Establishment

I. INTRODUCTION

Nickel is widely used in ferrous alloys in order to provide radiation-resistant structural components of fusion and fission energy systems.[1] Approximately seventy percent of elemental nickel is ^{58}Ni. Thus, the interaction of neutrons with this isotope is of considerable applied importance. In particular, the neutron scattering cross sections of ^{58}Ni can significantly contribute to the neutron energy transfer in fission- and fusion-energy systems. It was an objective of this work to improve the theoretical and experimental understanding of the fast-neutron interaction with ^{58}Ni in order to meet the applied nuclear-data needs.

^{58}Ni is physically a relatively simple nucleus consisting of a closed, Z = 28, proton shell, and a closed neutron shell, N = 28, with the addition of two neutrons in the ($1p_{3/2}$, $0f_{5/2}$, $1p_{1/2}$) sub-shell.[2] The latter interact with the general shell-model potential, with the addition of a two-body interaction between them. Aspects of the fast-neutron interaction with ^{58}Ni display properties characteristic of significant direct reactions (e.g., the inelastic-neutron excitation of the low-lying levels). The nature of these direct interactions is not entirely clear as the target is neither a simple vibrator nor rotor. The quadrupole moment of the yrast 2^+ level is not zero, and the energy spacing of the low-lying level structure does not follow the J(J+1) rule. Thus, it is of interest to examine the observed interaction of fast neutrons with ^{58}Ni in order to improve the understanding of the obvious direct-reaction processes. Even a simple optical-statistical model, quantitatively describing the general trends of the interaction, has merit as it forms the basis for DWBA predictions, and it is of interest from the applied point of view as it is a convenient vehicle for the interpolation and extrapolation of many measured properties to provide essential nuclear data for engineering-design purposes.

There has been recent interest[3-6] in the interpretation of low-energy nucleon-induced processes, uniquely accessible to the neutron probe, in the context of the dispersion relation and its association with fundamental nuclear forces and the Fermi Surface Anomaly. The unbound optical potential should extrapolate to the bound-state regime and the shell-model potential in a continuous manner. In doing so, one should be able to unify the understanding of the neutron processes with the strengths of bound-state stripping and pickup reactions. The dispersion relation also implies energy-dependent geometries of conventional optical potentials. It has recently been shown[5] that the optical model of neutron elastic

scattering in this mass region is very specific to the particular target. The observed elastic scattering from adjacent nuclei frequently differs by large amounts that are not consistent with "global" or even "regional" optical models. The effects are most evident at relatively low energies (e.g., at and below the Coulomb barrier), and thus primarily in neutron-induced processes where only a few channels are open. These differences are sensitive to the details of the imaginary potential, which reflect the specific nuclear structure of the targets involved. They also appear to be sensitive to the scattering reorientation processes, due to strong channel couplings (notably rotational coupling).[7]

There have recently been several studies of neutron scattering and polarization from ^{58}Ni, extending from ≈ 10 MeV to as much as 80 MeV.[8-11] The resulting models give reasonable representations of observed neutron total, and elastic-scattering cross sections, and of polarizations (particularly above 10 MeV). However, they are not always consistent, and there remain discrepancies, particularly between measured and calculated inelastic-scattering cross sections. The models have used both DWBA and coupled-channels methods to account for coupling of ground and first-excited, 2^+, levels. The resulting β_2 deformation parameters are reported to be intermediate in size between those deduced from the electro-magnetic interaction and proton scattering[8,9], as is qualitatively consistent with the predictions of the core-polarization model.[12] At higher energies, the models introduce volume absorption at ≈ 10 MeV, with the strength increasing with energy in a manner that is not clearly defined. Below 10 MeV the models become less satisfactory; total and scattering cross sections are not well represented, and qualitative attempts to improve the situation have suggested rather sharp changes in both potential strengths and geometries.[10] Furthermore, the low-energy region is sensitive to the dispersion relationship which interrelates real- and imaginary-potential geometries and strengths. Assuming ^{58}Ni is either a vibrator or rotor, the low-energy scattering will change with the couplings between the various low-lying levels. Indeed, it has been shown that the common spherical optical-model (SOM) treatment of the neutron interaction with such targets will lead to unusual potential geometries[13] (e.g., an imaginary radius considerably smaller than the real radius, and an imaginary-potential strength that is either approximately constant, or decreasing, with energy). Furthermore, the coupling to the yrast 2^+ state can introduce energy-dependent structure in the real and imaginary potentials. These various properties are evident only at low energies, and thus are uniquely accessible to neutron studies. They may have been manifest for many years in the inconsistency of optical potentials in this mass region as derived from low- or high-energy observations. Provision of the low-energy experimental information necessary to resolve some of these

issues is not trivial as, at few-MeV energies, the respective cross sections fluctuate by large amounts due to partially-resolved compound-nucleus resonance structure. The acquisition of a quantitative energy-averaged data base, consistent with the concepts of the SOM and coupled-channels-model, requires very detailed measurements.

The present paper reports an extensive experimental study of the interaction of fast neutrons with ^{58}Ni, undertaken with the objective of resolving some of the above issues. Combined with previous work from this laboratory[14], a detailed experimental understanding of the total and scattering cross sections of ^{58}Ni is achieved up to incident energies of 10 MeV (Section III). This experimental information, extended to 24 MeV using five elastic-scattering distributions from the literature, is interpreted in terms of the SOM and coupled-channels models, including considerations of vibrational and rotational coupling schemes, and of the dispersion relationship (Section IV). The properties of these models are discussed in detail, and the models provide a quantitative vehicle for applied data predictions. In Section V, some physical implications of the measurements and their interpretations are outlined.

II. EXPERIMENTAL METHODS

Most of the experimental methods employed in the present work have been extensively used at the Argonne Tandem Dynamitron for a number of years. They are described in detail in refs. 15-19, thus only an outline of the methods is given here.

The measurements employed a single sample of metallic nickel, 2 cm in diameter and 2 cm long, enriched to 99+ atom/percent in the isotope ^{58}Ni. The sample contained a fractional atom/percent of carbon, but appeared otherwise to be chemically pure. The very small contribution from other nickel isotopes was ignored. Routine observations (e.g., balance measurements) indicated that the sample was of uniform density, but precise assay via destructive testing was not possible.

The neutron total cross sections were deduced from the observed transmission of a well-collimated neutron beam through the sample[20], using the rotating-sample method and fast-timing techniques, as described in ref. 15. Thick composite targets of lithium and beryllium were bombarded with $\approx$ 7.0 MeV deuterons to obtain an intense white-neutron spectrum at the sample, extending from low energies to more than 11 MeV. The source was pulsed with durations of $\approx$ 1 nsec

and a repetition rate of 1.0 MHz. It was surrounded with a massive shield, with an ≈ 1 cm diameter collimating aperture at a 0^{o} source-reaction angle. The ^{58}Ni sample was mounted on a wheel, with a number of other samples and a void position, ≈ 3 m from the source. The cylindrical axis of the sample was co-linear with the neutron beam. The wheel was rotated a number of times a minute in a stepping manner. One of the samples was always carbon, in order to verify the performance of the measurement system. The neutron detector was a proton-recoil scintillator placed ≈ < 19 m from the neutron source on the beam axis. The neutron flight path was measured to within several mm. Conventional timing techniques provided an overall time resolution of ≈ 2 nsec, as observed from the γ-ray flash from the target. Energy scales were determined from the measured flight times and distances, and verified by the observation of prominent and well known resonances (e.g., those in carbon[21]). The geometry was very good, and thus in scattering corrections were negligible. The neutron source was very intense so dead-time effects were a serious concern. Appropriate corrections were made by introducing random pulses into the measurement system.

The measurements of scattered-neutron angular distributions were made using the Argonne ten-angle scattering apparatus.[17-19,22] The D(d,n)^{3}He source reaction was used throughout these scattering measurements, with the deuterium gas contained in a cell ≈ 3 cm long. The gas pressure in the cell was adjusted to provide incident-neutron resolutions at the sample ranging from ≈ 50 to 200 keV. The mean energy of the neutron source was determined to ≈ ± 10 keV by control of the incident deuteron beam. Each of the ten neutron flight paths was ≈ 5 m long. Relative detector efficiencies were determined using the spectrum of neutrons emitted from a spontaneously-fissioning ^{252}Cf source.[23] The absolute normalization of these relative detector efficiencies was established at each measurement period by observing scattered neutrons from the well-known H(n,n) standard reaction[21] at each measurement period. The observed scattering results for both the ^{58}Ni and H (polyethylene) samples were corrected for multiple-event, incident-beam-attenuation, and angular-resolution effects using the methods of ref. 24. These methods involve Monte-Carlo calculations which were pursued through three iterations to obtain good convergence.

Inelastic-neutron excitation of higher-lying levels in ^{58}Ni was studied using a single flight path of 15.68 m. Again, the D(d,n)^{3}He reaction was used as a neutron source, but with a ≈ 1.5 cm long gas cell operating at deuterium pressures providing incident-neutron energy spreads at the scattering sample of ≈ 50 keV. The neutron source was enclosed in a massive concrete shield ≈ 1.5 m thick, with a

single precision collimated aperture at a scattering angle of 80^{o}. The neutron detector consisted of a square array of liquid scintillators ≈ 2.5 cm thick and 40 cm on a side. This detector array was placed within another large concrete shield with a minimum thickness of ≈ 0.5 m. The sensitivities of these detectors was determined in the same manner as described above for the ≈ 5 m measurements.

III. EXPERIMENTAL RESULTS

A. Neutron Total Cross Sections.

Six sets of neutron total cross sections were measured, extending from ≈ 1 to 10 MeV. The objective was to obtain precise cross-section values with a broad resolution consistent with that employed in the differential neutron-scattering measurements, and with the energy-averaged concept of the optical-statistical and coupled-channels models. The highest possible resolution was not specifically sought.

The six sets of results were binned into 10-keV energy intervals to 4 MeV, into 50-keV bins for energies from 4 to 6 MeV, and into 100 keV bins at higher energies. These binned results displayed considerable structure as illustrated in Fig. III-1. That figure also shows the very high-resolution results of Harvey[25], which are consistent with the present values. The measured values were further averaged over 100 keV to 6 MeV and by 150 keV from 6 to 10 MeV, with the results shown in Fig. III-2. The statistical uncertainties associated with these averaged values are small, generally < 1%. Systematic uncertainties are probably dominated by the above-cited sample uniformity which could not be assessed. A similar average of the values of ref. 25 is in excellent agreement with that of the present results, as indicated in Fig. III-2. There are only two other sets of data that are comparable with the present work. Boschung et al.[26] have reported two isolated values (at 5.05 and 5.58 MeV) that are in excellent agreement with the present work. Earlier work at this laboratory by Budtz-Jorgensen et al.[27], using monoenergetic-source techniques, led to results extending from 1.0 to 4.2 MeV. Broad averages of the results of ref. 27 are in good agreement with those of the present work, as illustrated in Fig. III-2. These four sets of experimental results were obtained with various experimental techniques (two using monoenergetic methods and two white-source methods), and with very different experimental resolutions (broad, intermediate and high resolutions), with energy-averaged results in good agreement over a wide energy range. This suggests that self-shielding effects at the energies of the present work are not a serious concern. Therefore, no analytical

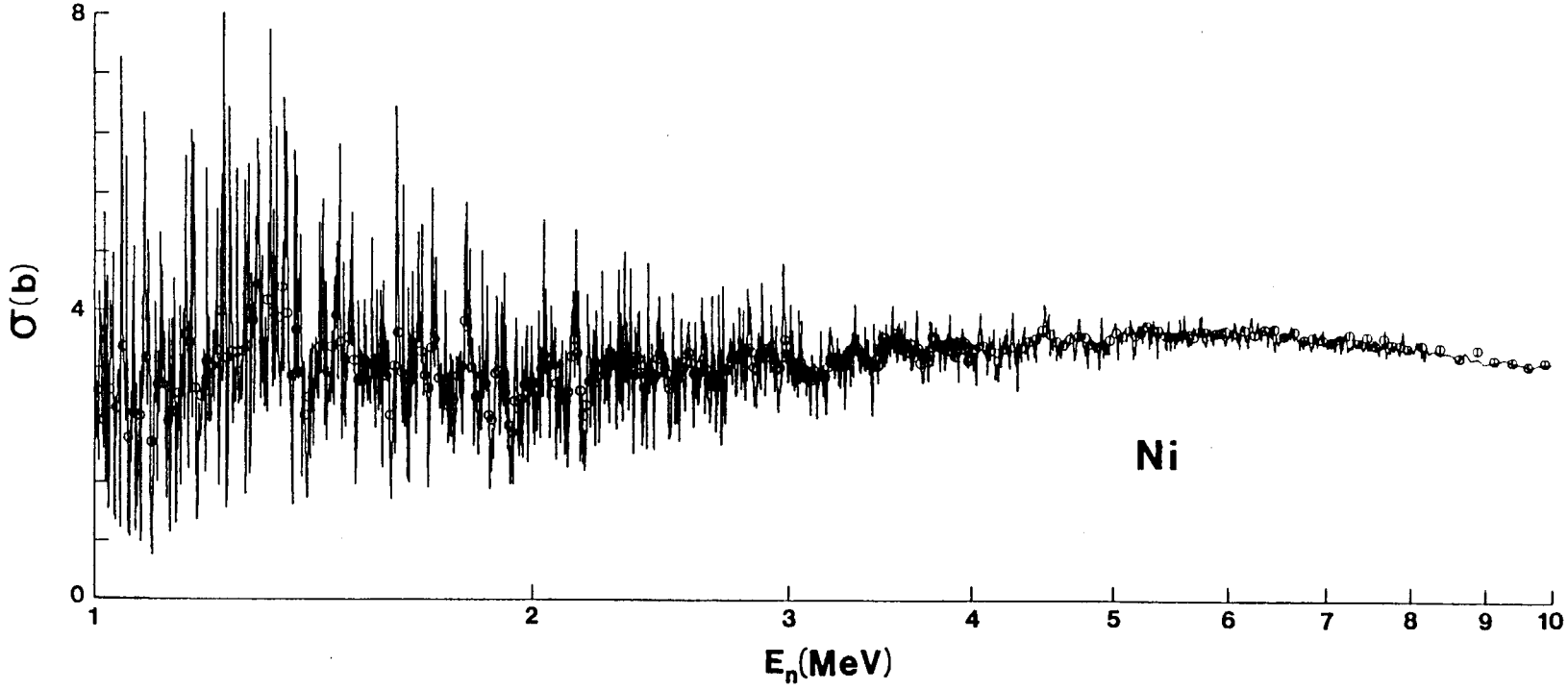

Fig. III-1. The present ^{58}Ni energy-binned experimental neutron total-cross-section results (symbol 0) compared with the high-resolution results of ref. 25 (curve).

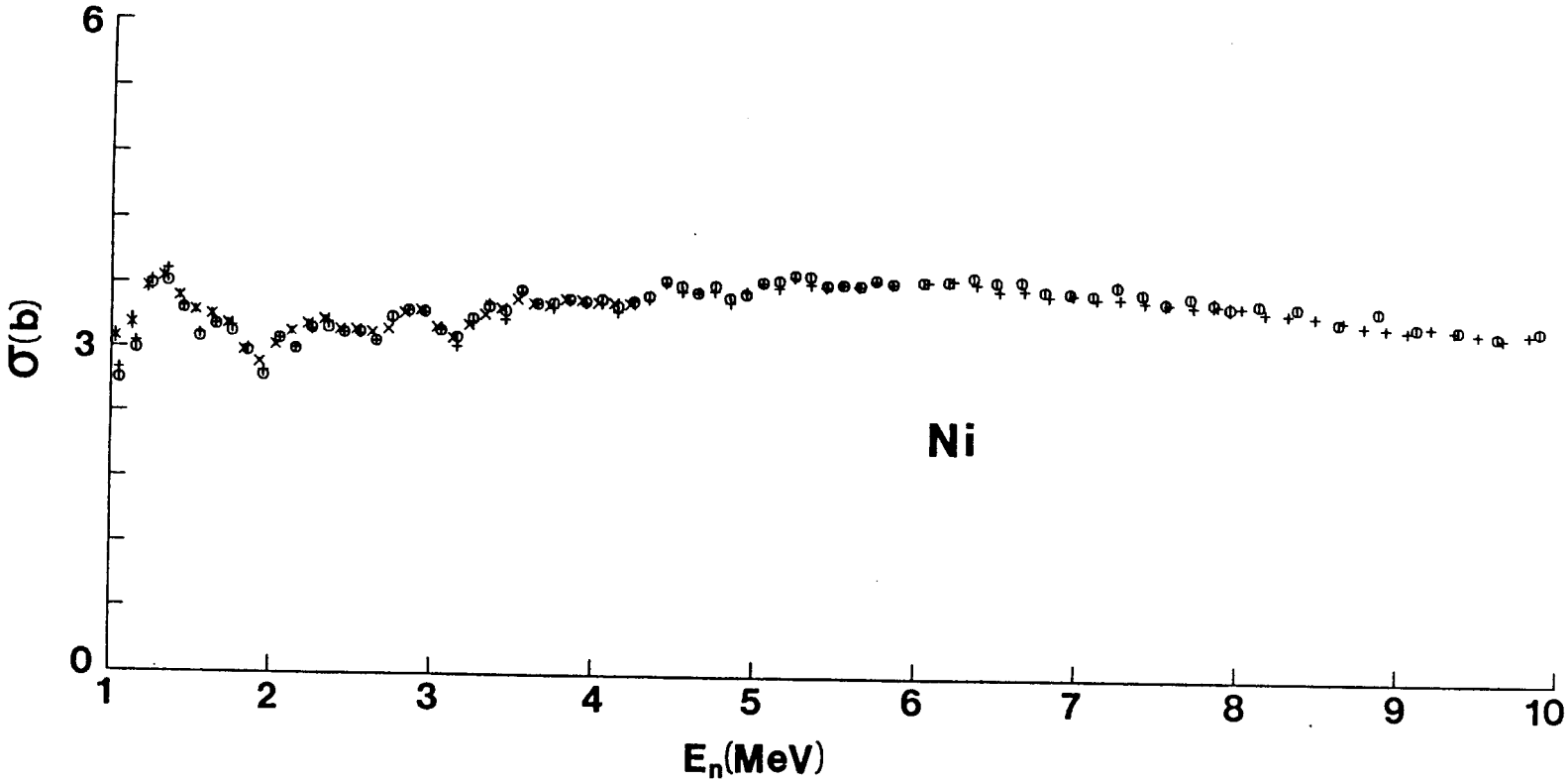

Fig. III-2. Comparison of broad energy averages of measured neutron total cross sections of ^{58}Ni. Data were averaged over 100 keV to 6 MeV and over 150 keV at higher energies. Symbols indicate the values derived from measurements as follows: 0 = present work, + = ref. 25, and X = ref. 27.

attempt was made to correct the present results for self shielding. Experimental corrections using various sample thicknesses were not possible due to the single sample available. Even in broad energy averages, consistent with the resolutions used in the differential scattering measurements, fluctuations in the total cross section persist to at least 5 MeV, and it is reasonable to expect these to be enhanced in the isolated exit channels (e.g., in the elastic-scattering channel). They are a concern in the interpretation discussed below.

B. Neutron Elastic-Scattering Cross Sections

The differential elastic-scattering cross sections were measured between $\approx 18^{0}$ and 160^{0}, from 4.5 to 10 MeV, in incident-energy intervals of $\approx$ 0.5 MeV. The number of differential values obtained at each incident energy ranged from $\approx$ 75 to more than 100. The statistical uncertainties of the measured values varied from less than a percent to more than 10%, depending upon the particular scattering angle and measurement period. Statistical and systematic uncertainties due to the hydrogen standard were relatively small (less than 1%). Systematic uncertainties associated with the Monte-Carlo correction procedures ranged from $\approx$ 1% to several percent, again depending upon the scattering angle. The relative scattering angles were believed known (from optical measurements) to $\approx 0.1^{0}$. The absolute values were determined to $\approx 0.2^{0}$. As a consequence, an uncertainty in differential cross sections was present, with a magnitude depending upon the scattering angle. Finally, as in all measurements, there may be unidentified uncertainty sources. They were subjectively estimated to be $\approx$ 0.5 mb/sr. These various uncertainty components were combined in quadrature to obtain the total uncertainty of the individual differential elastic-scattering values. The measurements were taken over several years, and the results were combined to obtain the final distributions at each energy, shown in Fig. III-3. The data obtained at these various measurement periods were generally consistent to within the above cited uncertainties.

There have been surprisingly few comparable elastic-scattering results reported in the literature. The lower-energy results of Budtz-Jorgensen et al.[27] extrapolate very nicely to the present results, as illustrated in Fig. III-3. Boschung et al.[26] have measured elastic-scattering cross sections of ^{58}Ni at $\approx$ 5.0 and 5.5 MeV. Their results are not as detailed as those of the present work, but the agreement is quite good, as illustrated in Fig. III-4. Guss et al.[8] have made elastic-scattering measurements at $\approx$ 8, 10, 12 and 14 MeV. Their results are generally consistent with the values of the present work to within the respective experimental uncertainties (e. g., see Fig. III-4). There are a number of elemental nickel

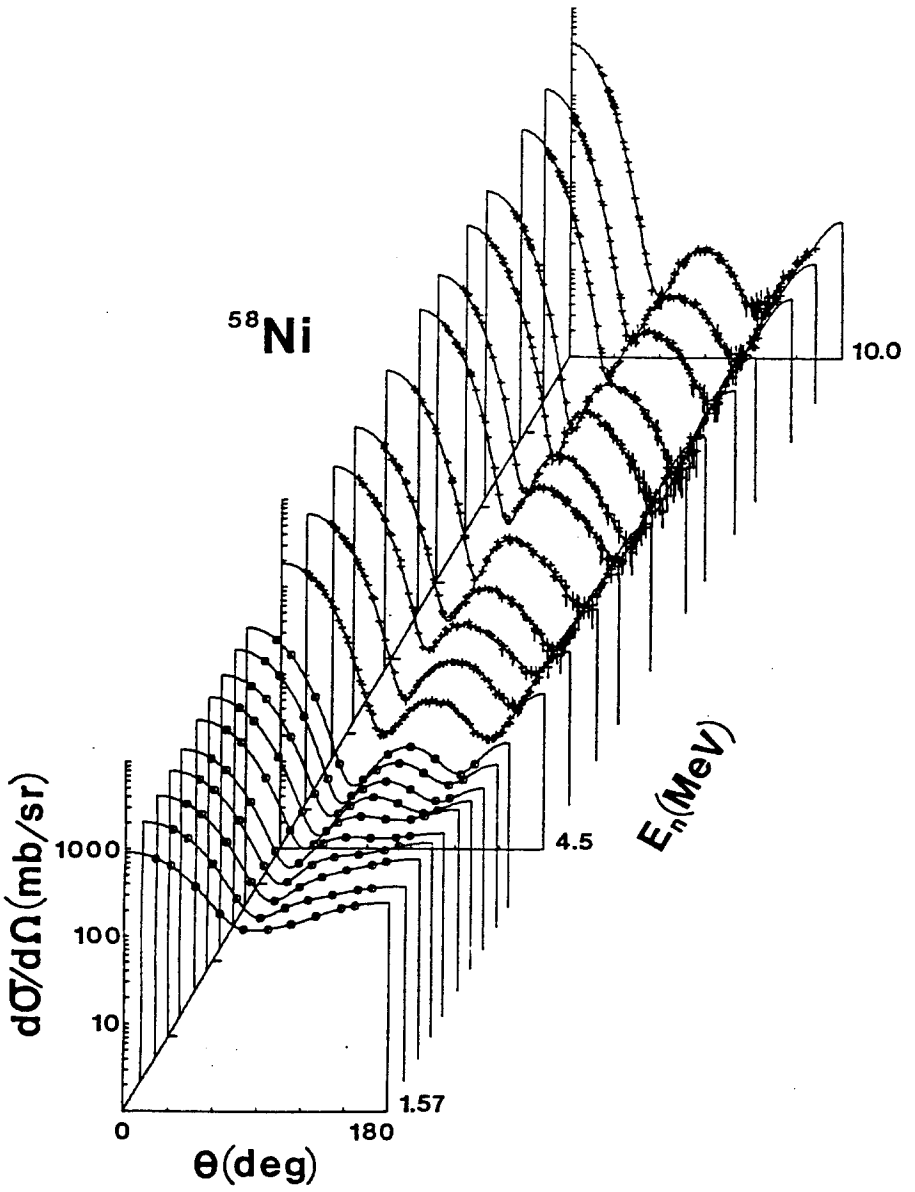

Fig. III-3. Differential elastic-scattering cross sections of ^{58}Ni. The present experimental results are indicated by "+" symbols. Approximately 200 keV averages of the lower-energy results previously obtained at this laboratory[27] are indicated by "0" symbols. Curves are eye-guides obtained by least-squares fitting a Legendre-polynomial expansion to the measured values. The data are in the laboratory coordinate system.

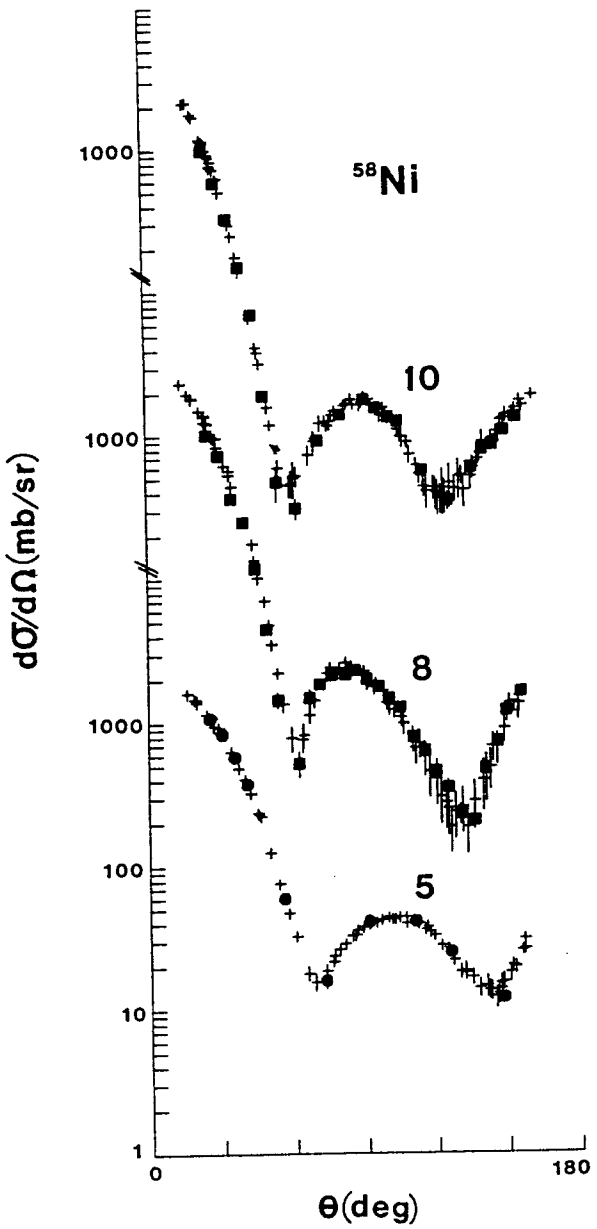

Fig. III-4. Some comparisons of differential elastic-scattering cross sections. The present results are indicated by "+" symbols, those of ref. 26 by "●" symbols, and those of ref. 8 by "■" symbols. The incident energies are ≈ 5, 8 and 10 MeV, as noted. The data are in the laboratory coordinate system.

elastic-scattering studies reported in the literature. However, approximately a third of the element consists of isotopes other than ^{58}Ni, having different level structures and deformations that may well influence the details of the elastic-scattering distributions at the energies of the present measurements. Therefore, direct comparisons with the present work are not possible.

C. Neutron Inelastic-Scattering Cross Sections

Most of the differential cross sections for the excitation of the 1.454 MeV 2^+ level were measured concurrently with elastic scattering using the ≈ 5 m flight paths. The measurements were made at ≈ 0.5 MeV incident-energy intervals from 4.5 to 10.0 MeV, and at fifty to more than one hundred scattering angles at each incident energy, distributed between ≈ 18^0 and 160^0. The experimental resolution was sufficient to resolve the inelastically-scattered component from the elastically-scattered neutrons at all but the very forward-scattering angles, where subjective judgments were used to strip the large elastic-neutron peak from the relatively small inelastic component (with a consequent compromise in accuracy). The uncertainties associated with the measured differential inelastic-scattering cross sections had the same origins as outlined above for the elastic scattering, but they were larger due to the relatively-small magnitudes of the cross sections (e.g., several mb/sr at some angles, and at higher energies). In addition, there are subjectively-estimated uncertainties associated with the resolution of the small inelastic-scattering components in the presence of the elastic-scattering contribution, which can be much larger. Generally, the total uncertainties ranged from ≈ 10% to more than 25%. The resulting differential cross sections are summarized in Fig. III-5 (for clarity the values have been averaged over ≈ 6^0 angular intervals), where the results below 4.5 MeV are ≈ 200-keV averages of prior work at this laboratory.[27] At selected higher energies, the present results are consistent with those of Boschung et al.[26] and of Guss et al.[8], as illustrated in Fig. III-6.

The differential-cross-sections of Fig. III-5 were least-squares fitted with Eq. III-1 to obtain the angle-integrated cross sections;

$$\frac{d\sigma}{d\Omega} = \frac{\sigma}{4\pi}\cdot\sum_{n=1}^{6}(1 + \omega_n\cdot P_n), \quad \text{(III-1)}$$

where P_n is the Legendre polynomial of order "n". (The method, of course, extrapolates beyond the experimental angular range. The results may be sensitive to the experimental forward-angle values,

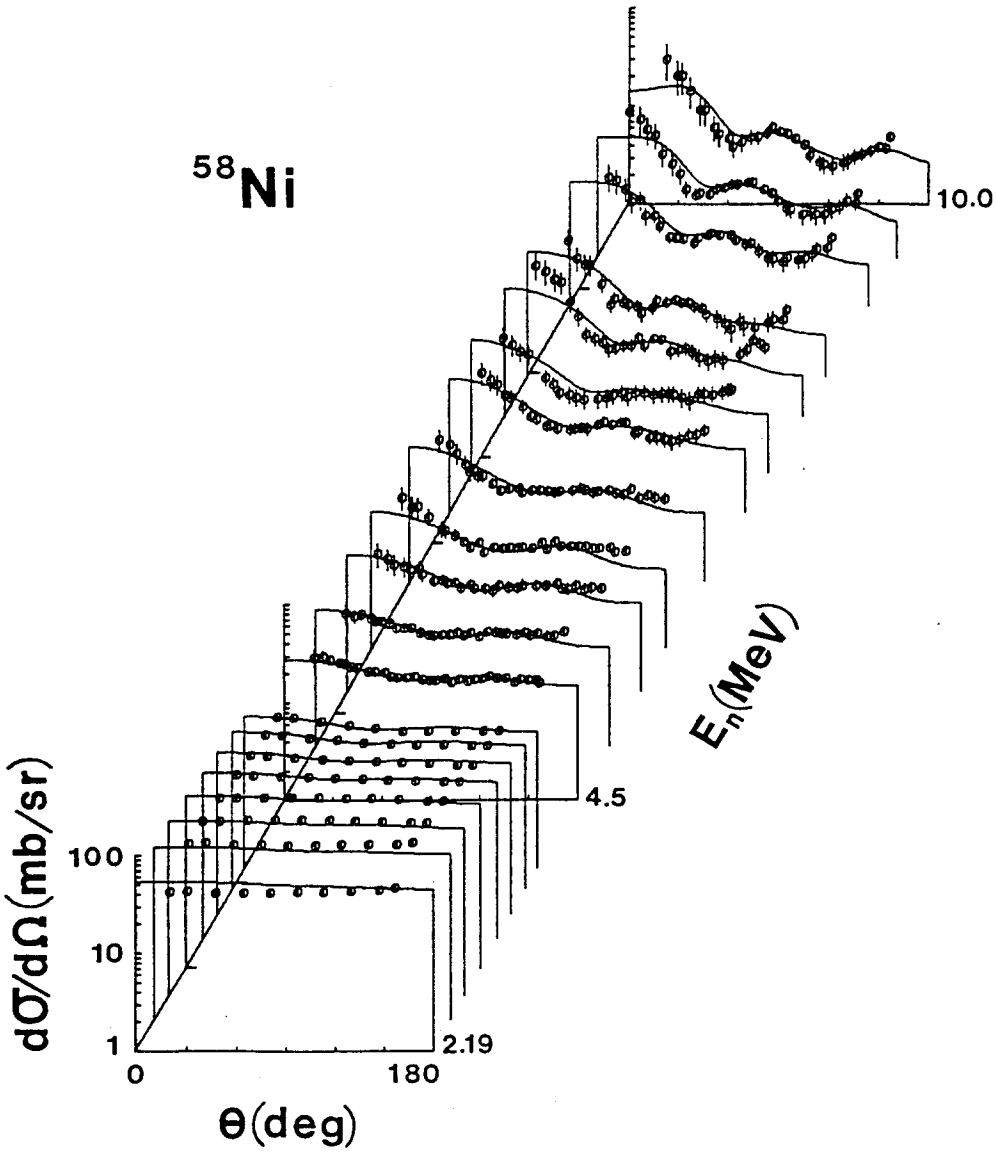

Fig. III-5. Differential neutron cross sections for the excitation of the 1.454 MeV level in ^{58}Ni. The experimental results are indicated by "O" symbols, and curves are from calculations as described in Section IV of the text. The present experimental results extend above 4 MeV, and an ≈ 200 keV average of the results of ref. 27 is given at lower energies. The data are in the laboratory coordinate system.

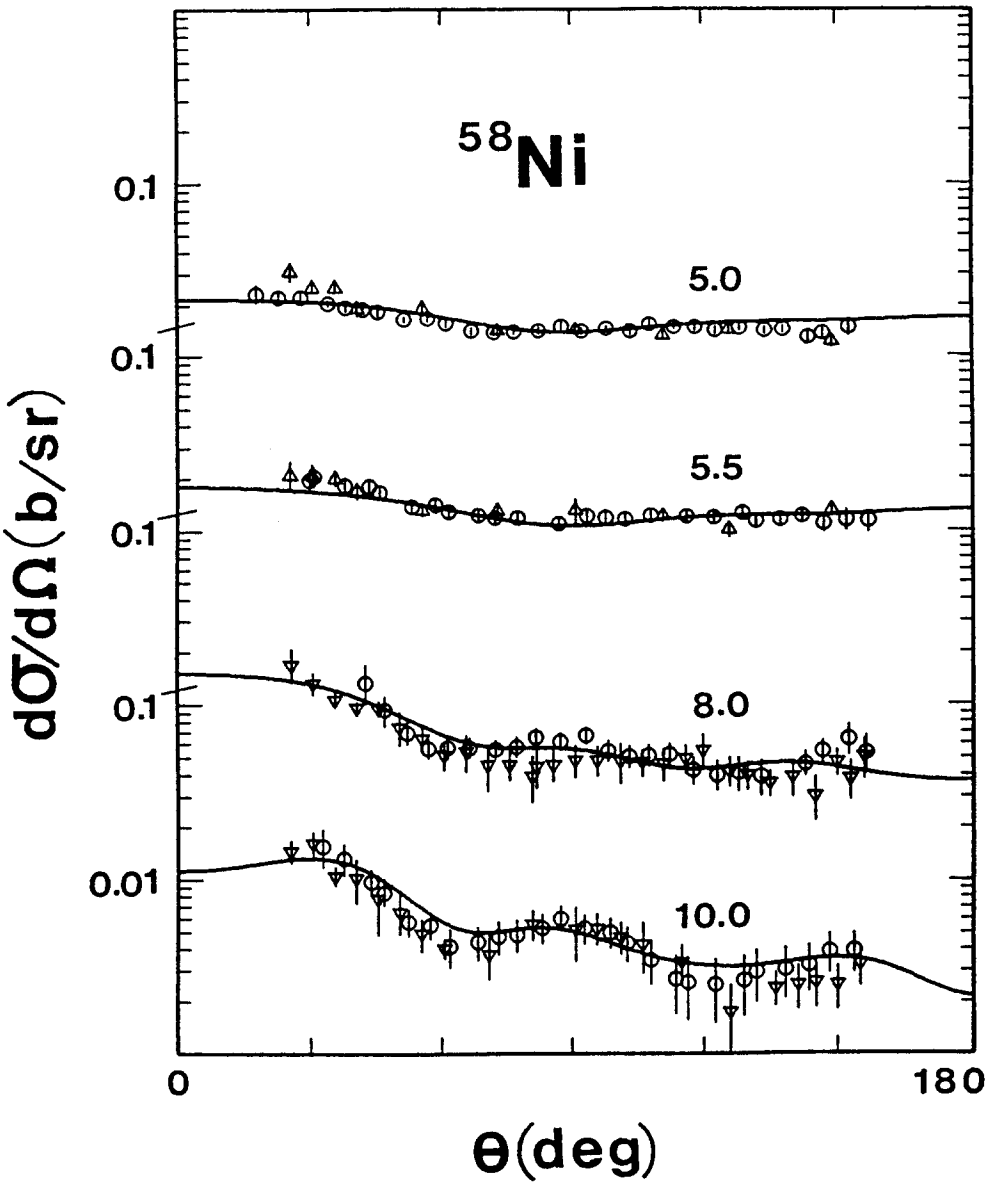

Fig. III-6. Comparisons of the differential cross sections for the excitation of the 1.454 MeV level in ^{58}Ni. The present results are given by "O" symbols, those of ref. 26 by "Δ", and of ref. 8 by "∇". Curves indicate the results of calculations as described in Section IV of the text. Approximate incident energies are numerically noted, and the data are in the laboratory coordinate system.

which are larger than some of model predictions of Section IV, and where the experimental uncertainties are relatively large.) The angle-integrated values, derived in this manner, are compared with previously-reported experimental results in Fig. III-7. The agreement with the present longer-flight-path results, discussed below, is good. The ≈ 5.0 and 5.5 MeV results of Boschung et al.[26] are in excellent agreement with the present values. The 8 and 10 MeV results of Guss et al.[8] are somewhat (≈ 10 - 20%) lower than the present values. This difference may be due to the fitting of the differential values (cited above) as the measured differential cross sections are very similar (see Fig. III-6). The extrapolation to the lower energy results of ref. 27 is very good. The higher-energy results of refs. 8 and 9 may be somewhat lower than suggested by the present work; again, possibly due to the fitting of the measured differential values. At energies above ≈ 8 MeV, this excitation cross section is certainly far larger (and with a different angular distribution) than predicted by compound-nucleus processes.

The cross sections for excitation of the higher-lying levels were examined at ≈ 5, 6, 7, and 8 MeV incident-neutron energies using the 15.68 m flight path at a scattering angle of 80^{o}. A representative time-of-flight spectrum, obtained using this arrangement, is shown in Fig. III-8. The elastic-neutron group and a number of inelastic-neutron groups are shown, together with the nominal observed excitation energies (in MeV). "C" refers to the contribution due to the small carbon contaminant in the sample. "γ" indicates the prompt-source γ-ray obscuring a small section of the spectrum at this particular energy. Partially-resolved neutron groups attributed to a composite of contributions are indicated with bars. A large number of inelastic-neutron groups are evident, and those attributable to the lower-energy excitations seem to be rather well resolved. Cross sections were deduced for 14 groups that are associated with the reported ^{58}Ni structure[28], as defined in Table III-1. The corresponding differential cross section values are given in Table III-2. The uncertainties associated with these cross sections were estimated, including considerations of counting statistics, experimental resolutions, and the other factors outlined above in the context of elastic scattering. They were generally 10% or larger, and knowledge of the cross sections becomes no more than qualitative at the higher-excitation energies due to uncertainties in the correlation of experimental resolutions with the underlying level structure. The long-flight-path differential values for the excitation of the 1.454 MeV level were converted to angle-integrated cross sections using the measured short-flight-path angular distributions. The results are in very good agreement with the short flight path values, as illustrated in Fig. III-7. It was assumed that the excitation of the higher-lying levels was governed by a compound-nucleus process (see Section IV), with the consequence that the angular distributions are symmetric about 90^{o}, and nearly isotropic. With this assumption, the 80^{o} differential values for the higher-lying states were converted to

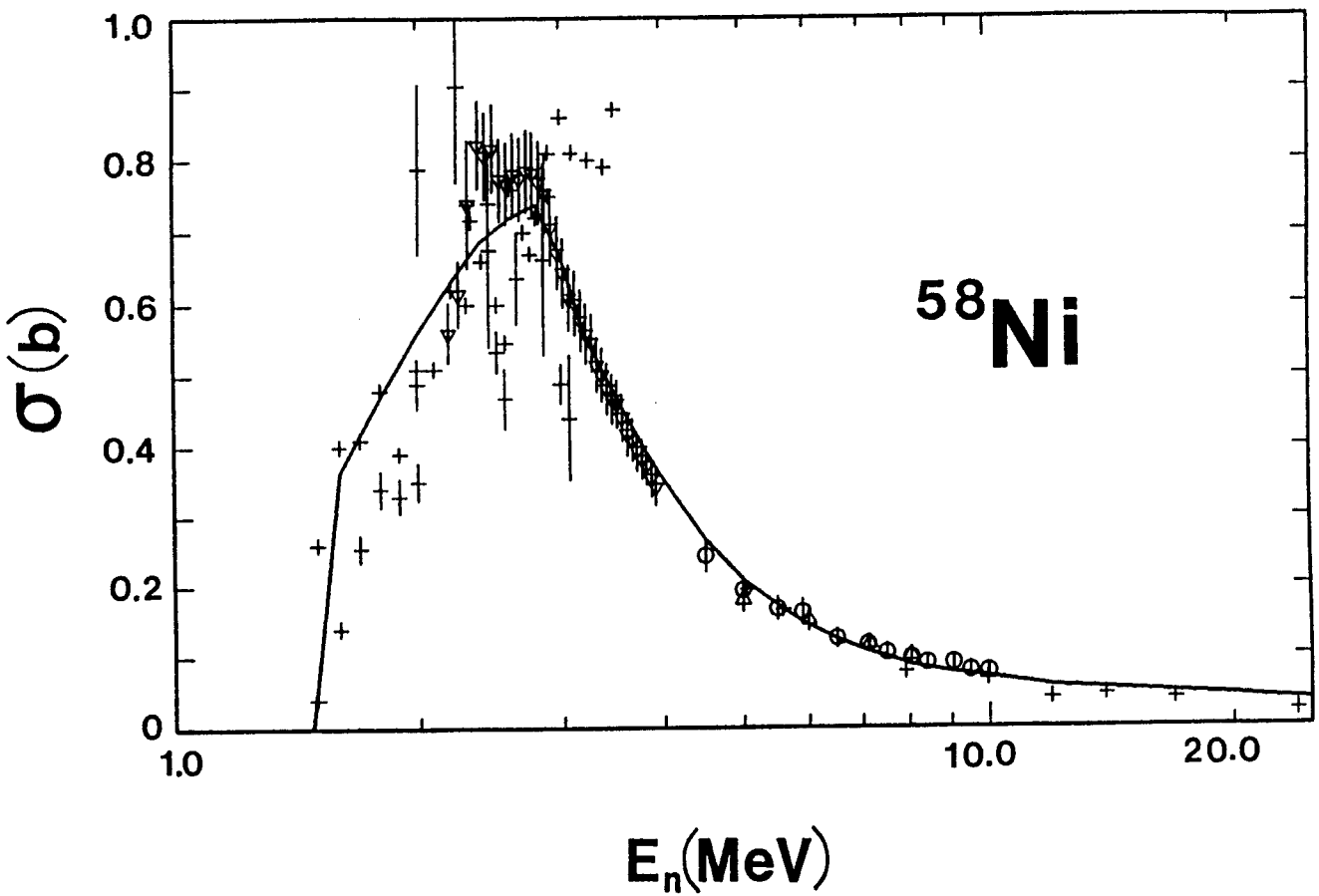

Fig. III-7. Angle-integrated cross sections for the excitation of the 1.454 MeV level in ^{58}Ni. The present ≈ 5 m results are indicated by "O", those from the present 15.68 m measurements by "Δ", and the lower-energy results of ref. 27 by "∇" symbols. Other values, taken from the files of the National Nuclear Data Center (Brookhaven National Laboratory), are indicated by "+". The curve shows the result of coupled-channels calculations, as described in Section IV of the text.

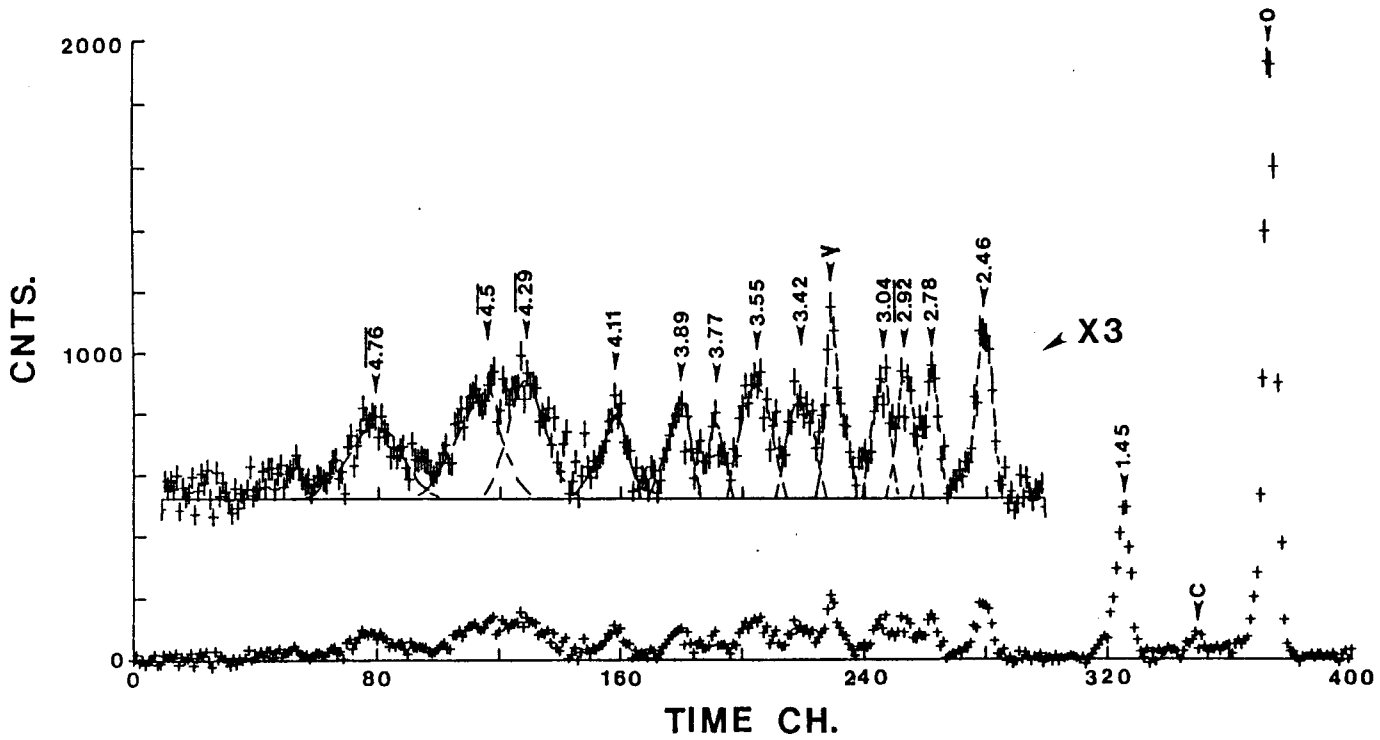

Fig. III-8. Time-of-flight spectrum obtained by scattering 8 MeV neutrons from ^{58}Ni over a flight path of 15.68 m and at a laboratory angle of 80^{0}. Numerical values indicate observed excitation energies in MeV, where there are bars over the numerical values they are attributed to the contributions of several neutron groups. "γ" indicates the target γ-ray, and "C" the elastic scattering from the small carbon contaminant of the sample.

Table III-1. Measured Inelastic-Excitation Energies in MeV.

No.	Observed	Reported in ref. 28
1	0.0	0.0 (0^+)
2	1.450 ± 0.020	1.454(2^+)
3	2.460 ± 0.030	2.459(4^+)
4	2.780 ± 0.030	2.776(2^+)
5	2.965 ± 0.030*	2.902(1^+)
		2.942(0^+)
		3.038(2^+)
6	3.220 ± 0.050	3.263(2^+)
7	3.360 ± 0.040	3.420(3^+)
8	3.520 ± 0.040*	3.525(4^+)
		3.531(0^+)
		3.558(?)
		3.593(1^+)
		3.620(4^+)
9	3.778 ± 0.050	3.774(3^+)
10	3.890 ± 0.050	3.898(2^+)
		3.932(?)
11	4.110 ± 0.100	4.108(2^+)
12	4.290 ≈± 0.100*	several(?)
13	4.500 ≈± 0.100*	several(?)
14	4.760 ≈± 0.100*	several(?)

* Indicates observed levels probably consisting of several components.

Table III-2. Differential inelastic excitation cross sections of ^{58}Ni measured at a scattering angle of 80^{o} using a 15.68 m flight path.

	Incident Energy (MeV)			
E_x(MeV)[a]	5	6	7	8
1.45	12.7[b]	10.2	7.1	5.9
2.46	5.5	5.6	3.0	1.8
2.78	5.8	5.9	2.0	1.5
2.97	12.2	7.5	2.1	2.0
3.22	-	4.5	2.9?	1.9
3.36	-	4.4	2.4	1.5
3.52	-	8.1	3.4	2.3
3.78	-	7.4	1.3	1.8
3.89	-	11.3?	2.1	-
4.11	-	-	2.8	7.3
4.29	-	-	5.8	
4.50	-	-	6.9	-
4.76	-	-	7.0	-

a. "Observed" values from Table III-1.
b. All cross sections in mb/sr.

angle-integrated cross sections, using the respective calculated angular distributions. The results for the first few of these higher-excited levels are shown in Fig. III-9. There is very little comparable prior-experimental information, particularly at incident energies above 4
eV where all the previous information comes from the work of Boschung et al.[26] The agreement with the present values is qualitative when consideration is given to the respective experimental resolutions in the context of the underlying structure. The present results also reasonably extrapolate to the lower-energy results of ref. 27.

IV. INTERPRETATION

A. The Experimental Data Base.

The model interpretations considered the following experimental data:

i) The s- and p-wave strength functions deduced from low-energy resonance data as given in the compilation of ref. 29.

ii) The energy-average neutron total cross sections given in the evaluation of ref. 30. That evaluation includes the present experimental results as a part of the input.

iii) The ≈ 1.5 to 3.9 MeV neutron elastic-scattering results of ref. 27. This data set, previously obtained at this laboratory, is very detailed, and displays fluctuations due to partially-resolved resonance structure. Therefore, the experimental results were averaged over ≈ 200 keV incident-neutron-energy intervals in order to smooth the fluctuations and, at the same time, reduce the experimental information to a more manageable size for the extensive numerical fitting procedures. The energy-averaged distributions are shown in Fig. III-3 below 4 MeV.

iv) The neutron elastic-scattering results of the present work, extending from 4.5 to 10 MeV.

v) The neutron elastic-scattering results of ref. 8 at 12 and 14 MeV, and those of ref. 10 (from the same institution) at 16.9 MeV.

vi) The neutron elastic-scattering results of ref. 11 at 21.6 MeV. These are elemental results (68.27% ^{58}Ni), but appear to be of good quality, and thus provide a very useful data set above 20 MeV.

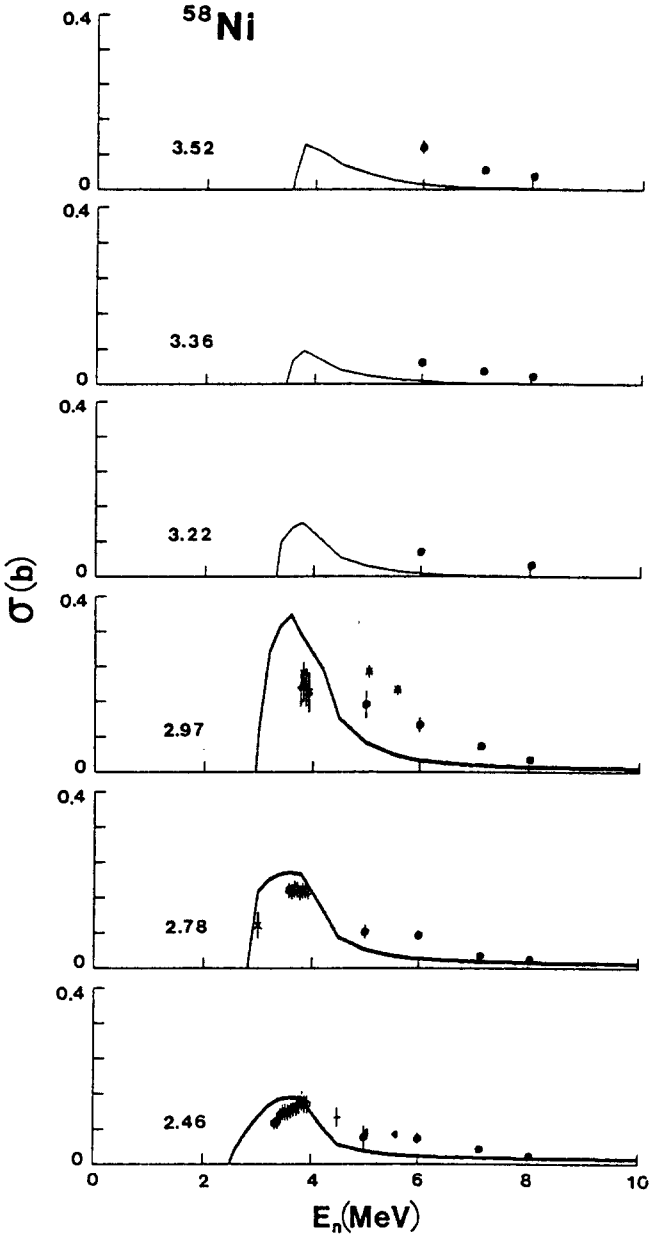

Fig. III-9. Angle-integrated inelastic-scattering cross sections of ^{58}Ni for excitations above 2 MeV. The present results are indicated by "●", those of prior work at this laboratory[27] by "○", and literature results, as compiled by the National Nuclear Data Center (Brookhaven National Laboratory), by other symbols. Heavy curves indicate the results of calculations including both compound-nucleus and direct-reaction contributions, and light curves only the compound-nucleus component, as discussed in the text. The respective observed excitation energies are numerically indicated in MeV.

vii) The final component of the data base was the 24-MeV neutron elastic-scattering data of ref. 9.

Most of the experimental information was available in numerical form from the National Nuclear Data Center. An exception was the results of ref. 11, which were available only in the form of a published figure at the time of the interpretations. In addition, consideration was given to the inelastic excitation of the yrast 2^+ excited level as cited in the following discussion.

B. Phenomenological Spherical Optical-Statistical Model (SOM).

A SOM was deduced with the objectives of; i) providing a basis for the subsequent construction of a dispersive SOM and coupled-channels models including collective effects, ii) giving general guidance as to the physical features of the neutron interaction with ^{58}Ni, and iii) making available a relatively simple phenomenological model for applied use. The SOM derivation was based upon the elastic-scattering data outlined above, with subsequent subjective considerations of the low-energy strength functions and the total cross section. The SOM interpretation is fraught with a number of problems. ^{58}Ni displays collective properties (e.g., the character of the cross sections for the inelastic-neutron excitation of the yrast 2^+ state, and the enhanced B(E2) value for that state[28]), thus the SOM can only be a qualitative approximation. More correct coupled-channels interpretations are discussed below. ^{58}Ni is a relatively light even-even nucleus. Fluctuations are evident in the observed neutron total cross section to $\approx$ 5 MeV or more (see Fig. III-2), even in a relatively broad energy average, and may extend to higher energies in the elastic-scattering channel. They are certainly evident in the few-MeV region in the elastic-scattering data shown in Fig. III-3. Such fluctuations are not consistent with the basic concept of the SOM. The excited level structure is reasonably well known to approximately 3.5 MeV[28], but at higher energies the density of levels becomes large and knowledge of their spins and parities is uncertain. The elastic-scattering data above 10 MeV is sparse, limited to only five elastic-scattering distributions from different sources (the various results do not appear to be entirely consistent). From $\approx$ 1 to 10 MeV (the range of results from this laboratory) the interpretation is particularly difficult as the elastic distributions are relatively structureless (with only two broad minima), and the cross sections fall with angle by approximately three orders of magnitude, to the first minimum at $\approx 60^0$, with a concurrent increase in the experimental uncertainty of more than an order of magnitude. Below 10 MeV, the experimental uncertainties are reasonably defined (by the present work and that of ref. 27). At higher energies, the data comes from a variety of sources, and the uncertainties cited appear to be largely due to statistical contributions. There may be

additional and significant errors as; for example, those associated with scattering-angle uncertainties.

The SOM derivation (and the entire discussion of this paper) assumes a Saxon-Woods real potential, a Saxon-Woods-derivative imaginary potential, and a Thomas real spin-orbit potential.[31] Throughout this paper, an imaginary spin-orbit potential was ignored, as detailed polarization studies show little, or no, evidence for it.[8,10] Compound elastic-scattering contributions were explicitly considered to 8.0 MeV, using the Hauser-Feshbach formulation[32], corrected for resonance width fluctuations and correlations using the method of Moldauer.[33] Twelve discrete levels (inclusive of the g.s.) were considered to excitations of ≈ 3.6 MeV, with energies, spins and parities taken from ref. 28. Higher energy excitations were represented using the statistical formulation of Gilbert and Cameron.[34] At 8 MeV and above, the elastic scattering was assumed to be entirely due to shape scattering. All SOM parameter derivations were based upon explicit chi-squares fitting of the elastic-scattering data using the optical-model code ABAREX.[35] These are non-linear fitting procedures which are sensitive to the uncertainty specification, and that is not clearly defined above 10 MeV. The experimental data are best known where the cross sections are large, and are far more uncertain in the deep minima of the distributions. Thus chi-squares fitting will not necessarily give a detailed description of the minima of the distributions, or of ratios of distributions (as discussed in ref. 36).

In the SOM fitting, it was assumed that the spin-orbit potential was given by

$$\begin{aligned} V_{so} &= 5.5 \text{ MeV} \\ r_{so} &= 1.0 \text{ fm} \\ a_{so} &= 0.65 \text{ fm}, \end{aligned} \qquad \text{(IV-1)}$$

where V_{so} is the strength, r_{so} is the reduced radius (herein all radii are expressed in the form $R_i = r_i \cdot A^{1/3}$), and a_{so} is the diffuseness. This spin-orbit potential is similar to that reported for this mass region [8,10], and it results in a reasonable description of the observed polarizations, as outlined below.

Attention was given first to the geometry of the real potential as it is reasonable to expect it to be relatively insensitive to detailed nuclear-structure effects. With the spin-orbit potential fixed to the values of Eq. IV-1, the chi-squares fitting started by

concurrently varying the six parameters: real and imaginary strengths, radii and diffusenesses. The resulting real diffuseness, a_v, was essentially energy independent and not strongly correlated with either the real-potential strength or radius. The average value of a_v (see Table IV-1) was accepted, and the chi-squares fitting repeated, varying the remaining five parameters. The resulting real-potential radius decreased with energy in a manner well represented by the linear expression of Table IV-1. This behavior is qualitatively consistent with the predictions of nuclear-model calculations, and with those of SOM's reported in similar mass-energy regions.[37,38]

With the real-potential geometry fixed to the values of Table IV-1, four-parameter chi-squares fits were carried out. The resulting imaginary radius, r_w, is strongly energy dependent, falling from a large value at zero energy to approximately a constant value at E ≈ 4.7 MeV. This energy dependence is reasonably well represented by the two linear segments given in Table IV-1. The energy-dependent behavior of r_w is unusual, and this implies that low- and high-energy models will be quite different. With r_v, a_v and r_w fixed to the values of Table IV-1, three parameter fits were carried out to determine the imaginary diffuseness, a_w. The resulting a_w increases rapidly with energy, rising from a small value of ≈ 0.26 fm as E increases from 0, in an approximately linear manner, as given in Table IV-1. a_w is strongly correlated with the imaginary strength.

The final step in the fitting varied the real and imaginary potential strengths, with the geometries fixed to the values of Table IV-1. The resulting potential strengths, expressed in terms of volume-integrals-per-nucleon,

$$J_i = \frac{4\pi}{A} \int V_i(r) \cdot r^2 \, dr, \qquad \text{(IV-2)}$$

are shown in Fig. IV-1. The general trend of the real-potential strength is a linear decrease with energy. Superimposed on this general trend is a pronounced minimum centered at about ≈ 4 MeV. A number of alternate approaches to the SOM fitting were examined in an effort to remove this minimum, with no success. Thus, it was concluded that the minimum was not an artifact of the fitting procedure. The imaginary strength, J_w, falls with energy up to ≈ 10 MeV, and then remains nearly a constant of relatively large magnitude. This behavior is reasonably well represented by the two linear segments of Table IV-1. The structure in J_v, and the energy dependence of J_w, shown in Fig. IV-1, are unusual, and the possible physical implications are discussed in Section V. At this point, it suffices to note that the SOM parameterization of Table IV-1 describes

Table IV-1. ^{58}Ni SOM parameters deduced by chi-squares fitting the measured elastic-scattering distributions with their experimental uncertainties.[a,b] The incident neutron energy, E, is in MeV.

Real Potential

$$a_V = 0.6461 \quad \text{fm}$$
$$r_V = (1.305 - 0.006 \cdot E) \quad \text{fm}$$
$$J_V{}^{c} = (512.0 - 6.02 \cdot E) \quad \text{MeV-fm}^3$$

Imaginary Potential

$$a_W = (0.26 + 0.02 \cdot E) \quad \text{fm}$$
$$r_W = (1.50 - 0.07 \cdot E) \quad \text{fm} \qquad (E < \approx 4.7)$$
$$= (1.160 + 0.002 \cdot E) \quad \text{fm} \qquad (E > \approx 4.7)$$
$$J_W = (133.0 - 3.9 \cdot E) \quad \text{MeV-fm}^3 \qquad (E < \approx 10)$$
$$= 94.0 \quad \text{MeV-fm}^3 \qquad (E > \approx 10)$$

a. Assuming the spin-orbit potential of Eq. IV-1.
b. Throughout this report potential parameters are given with sufficient accuracies to permit the reconstruction of the illustrated results. The precisions do not necessarily imply parameter uncertainties.
c. General linear trend as per the text.

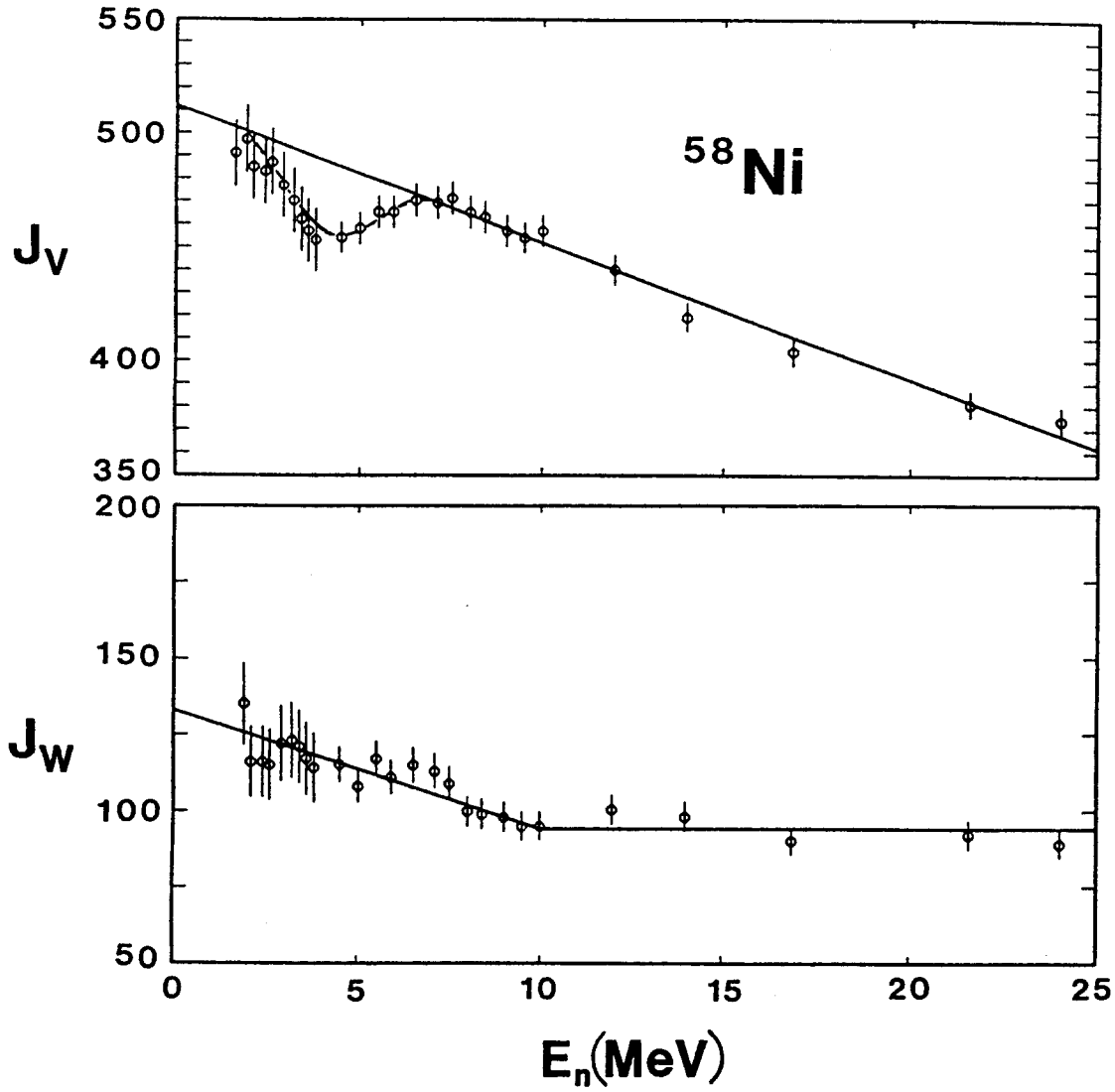

Fig. IV-1. Real (J_v) and imaginary (J_w) SOM potential strengths expressed as volume-integrals-per-nucleon (in units of MeV-fm^3). The results of the fitting procedures described in the text are shown by symbols. Solid curves indicate the linear parameterizations of Table IV-1, and the dashed line is an eye guide.

the data base from which it was constructed fairly well, as illustrated in Fig. IV-2.

It was pointed out above that the chi-squares fitting can be sensitive to experimental uncertainties, and that the uncertainties are not well known above 10 MeV. This sensitivity was examined by repeating the above fitting procedures assuming all experimental uncertainties were identical (i.e., equal weight for each data point). As expected, an arguably improved description of the minima of the distributions (where the experimental uncertainties are large) was obtained, but the SOM parameters did not substantively differ from those given in Table IV-1.

Table IV-1 and Fig. IV-1 define a SOM that should be reasonably applicable for the calculation of many of the energy-averaged properties of the neutron interaction with ^{58}Ni up to at least 24 MeV, and thus serve as a good vehicle for many applications, and as a suitable starting point for more detailed model investigations (e.g., DWBA calculations). The differential elastic-scattering cross sections are reasonably described, as illustrated in Fig. IV-2. The calculated strength functions are $s_0 = 2.34 \times 10^{-4}$ and $s_1 = 0.781 \times 10^{-4}$, in acceptable agreement with those deduced from resonance measurements (as complied in ref. 29) of $(2.8 \pm 0.6) \times 10^{-4}$ and $(0.5 \pm 0.1) \times 10^{-4}$, respectively. Calculated neutron total cross sections are compared with the measured values in Fig. IV-3, and the agreement is reasonably good up to at least 20 MeV, with differences of only a few percent or less (largely centered about $\approx$ 6 MeV), except at lower energies where the fluctuations persist even in broad averages of the experimental values. The SOM derivation started with the a-priori assumption of the spin-orbit potential given in Eq. IV-1. The choice was suitable as the calculated polarizations (e.g., at 10 MeV) described the major features of the corresponding measured values of ref. 8. Certainly, the potential of Table IV-1 is not valid at very high energies as the energy dependencies of several of the parameters will lead to unfortunate results. An energy-asymptotic approach to approximately constant values above $\approx$ 24 MeV is far more appropriate.

Aspects of the above SOM, and their physical implications are discussed in Section V. However, some of the qualitative features are pointed out at this time as they were further investigated with the fitting procedures. The real potential diffuseness, a_v, is not unusual, being constant with energy and of a commonly encountered magnitude. The real-potential radius slowly decreases with energy. Similar behavior is commonly observed (e.g., ref. 37), and is generally consistent with fundamental nuclear-matter concepts.[38] Above $\approx$ 7 MeV the real-potential strength (J_v of Fig. IV-1) decreases

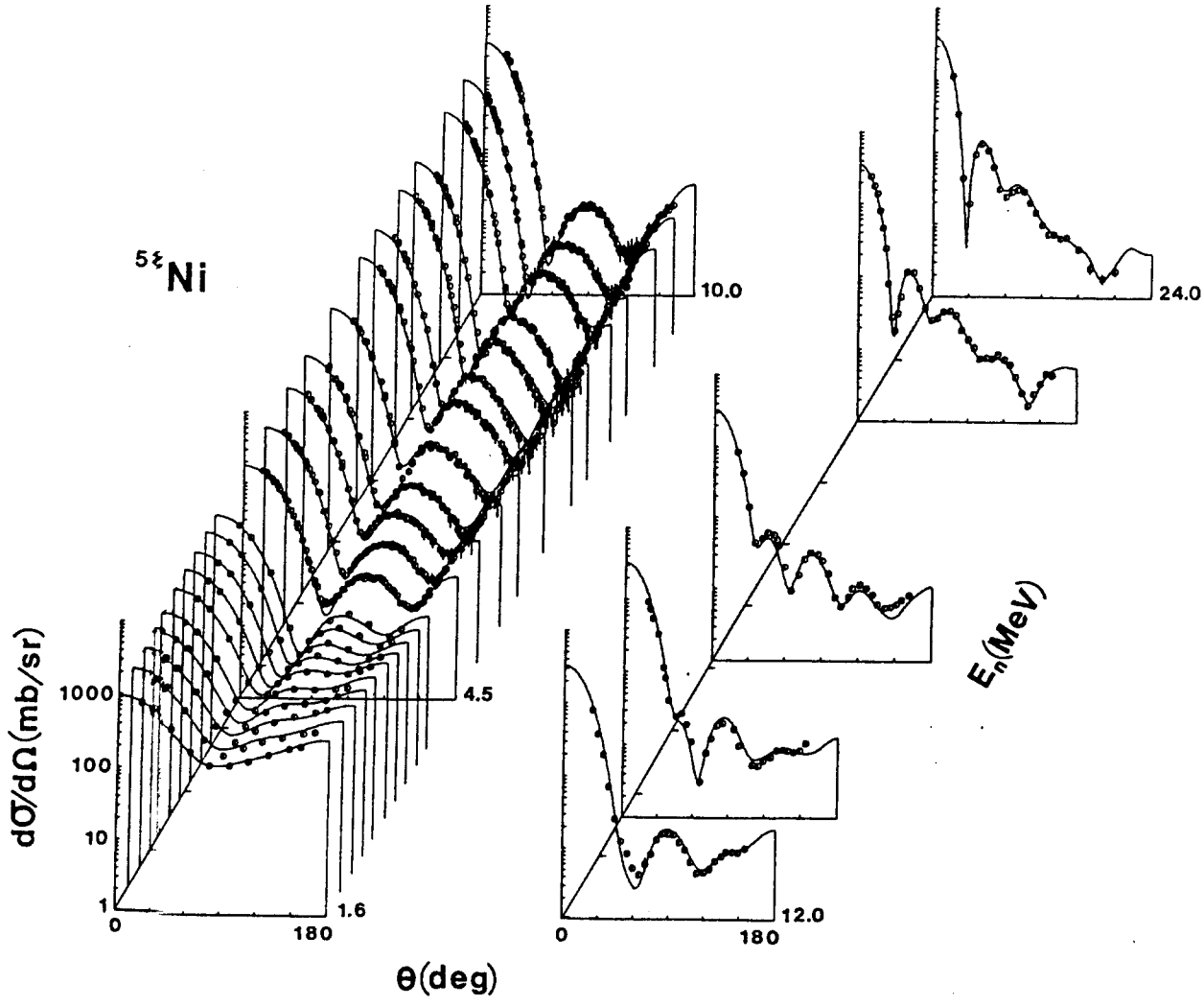

Fig. IV-2. Differential elastic-scattering cross sections of ^{58}Ni. Experimental values are indicated by symbols. Curves indicate the results of SOM calculations using the geometries of Table IV-1 and the strengths of Fig. IV-1, including the structure in J_v indicated by the dashed line. The data are given in the laboratory coordinate system.

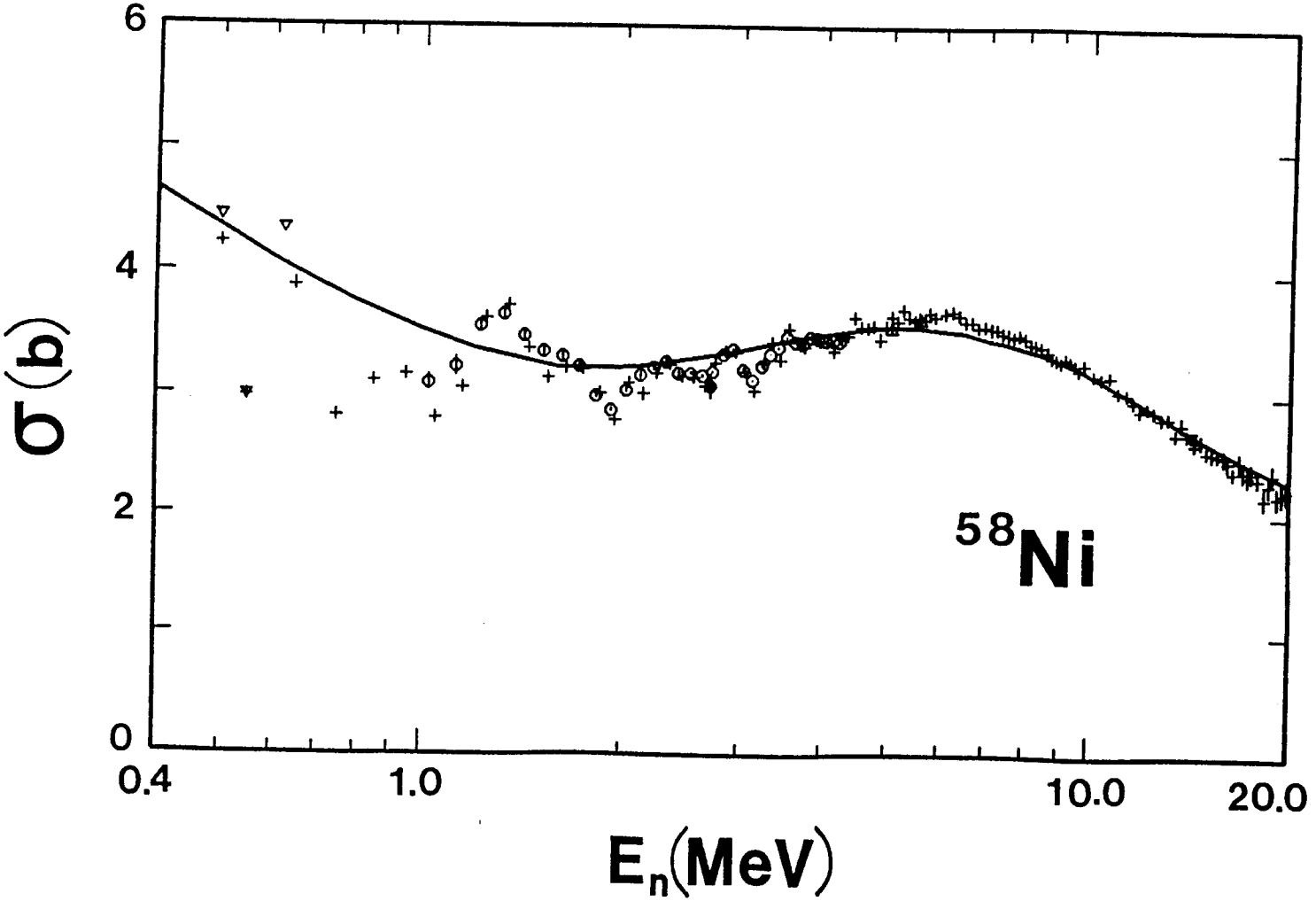

Fig. IV-3. Comparison of measured and calculated neutron total cross sections of ^{58}Ni. Symbols indicate energy averages of measured values.[30] The curve denotes the results of SOM calculations as described in the text.

linearly with energy in a manner consistent with the predictions of Hartree-Fock calculations. Below ≈ 7 MeV, there is a pronounced dip in the magnitude of J_v, centered about 4 MeV. This dip extends from the upper limit of the detailed knowledge of excited levels in ^{58}Ni to energies where compound-elastic scattering becomes very small, and the elastic scattering must be essentially entirely due to shape-elastic processes. This suggests that the anomaly in J_v may be due to inappropriate calculation of compound-elastic contributions at relatively low energies where the statistical description of ref. 34 may not be particularly reliable. This possibility was investigated by refitting the data with a wide range of temperatures in the formalism of ref. 34, with no improvement in chi-square or in the subjectively-judged "goodness" of the fits to the distributions. Of course, underlying all of the interpretations at lower energies is the assumed validity of the Hauser-Feshbach formula, as augmented by Moldauer.

Above ≈ 5 MeV, the imaginary-potential radius, r_w of Table IV-1, is nearly energy independent, and between ≈ 5 - 10 MeV, it is significantly smaller than the real radius, r_v. The latter property has been shown to be characteristic of fitting elastic scattering from a collective vibrational nucleus with a SOM.[13,39] Below ≈ 5 MeV, r_w sharply increases with decreasing energy. This is a very unusual behavior, but one that results in $r_w > r_v$ as $E_n \rightarrow 0$, as is characteristic of low-energy SOMs largely based on strength-function interpretations.[40] The imaginary-potential diffuseness linearly increases with energy in a manner that has previously been observed in this mass-energy region.[37] This behavior suggests that the surface absorption becomes more diffuse as the energy increases in a physically rational manner. It is common practice in "global" SOMs to introduce a volume-absorption potential at about 10 MeV to qualitatively account for such a trend.[41] A similar procedure was tried in the present work, but the fits to the higher-energy distributions were not significantly improved, nor did the introduction of a simple volume absorption tend to reduce the diffuseness of the surface absorption. This suggests that the expected trend toward volume absorption with increasing energy is, in the present energy range, more of a broadening and tailing toward the nuclear interior of the surface absorption rather than the onset of entire volume absorption. The imaginary-potential strength of the present SOM is nearly constant with energy above ≈ 10 MeV, but increases as the energy decreases from 10 MeV. This is contrary to the generally-increasing imaginary strength with energy to ≈ 10 MeV followed by slowly decreasing values at higher energies as characteristic of many "global" SOMs.[41] Again, it has been shown that the behavior of the imaginary-potential strength encountered in the present work can be, in part, the result of using a simple SOM to

describe the neutron interaction with a collective vibrator.[13,39] Finally, the present interpretation uses the a-priori spin-orbit potential of Eq. IV-1, and with it the description of measured polarizations is reasonable. However, alternate choices were examined by re-fitting the elastic-scattering cross sections with a reasonable range of spin-orbit strengths. There was no significant improvement in the comparison of measured and calculated values and, frequently, a deterioration. In particular, the somewhat different spin-orbit potential used in the vibrational model, below, did not significantly alter the spherical interpretation.

C. The Dispersive Optical Model (DOM)

The real, V, and imaginary, W, parts of the SOM are related through the dispersion relationship[42],

$$V(r,E) = V_{HF}(r,E) + \frac{P}{\pi}\int_{-\infty}^{+\infty}\frac{W(r,E')dE'}{(E-E')}, \qquad \text{(IV-3)}$$

where P denotes the principal value of the integral, and V_{HF} the Hartree-Fock potential. This relationship leads to the so-called "Fermi Surface Anomaly", which results in a departure of the real-potential strength from V_{HF} at low energies. It is conceivable that the unusual energy dependence of J_V obtained using the SOM (see Fig. IV-1) and some of the energy dependencies of the geometries are a manifestation of this anomaly. This possibility was examined by re-fitting the experimental data using the DOM.

As the SOM parameters are energy dependent, it is convenient to reformulate Eq. IV-3 in terms of potential strengths expressed as volume-integrals-per nucleon, J_i. Eq. IV-3 then takes the form

$$J_V(E) = J_{HF}(E) + \frac{P}{\pi}\int_{-\infty}^{+\infty}\frac{J_W(E')dE'}{(E-E')}\cdot dE'. \qquad \text{(IV-4)}$$

The integral can be broken into surface, dJ_S, and volume, dJ_{VO}, contributions, where

$$dJ_S(E) \equiv \frac{P}{\pi}\int_{-\infty}^{+\infty}\frac{J_S(E')dE'}{(E-E')}$$

and (IV-5)

$$dJ_{VO}(E) \equiv \frac{P}{\pi}\int_{-\infty}^{+\infty}\frac{J_{VO}(E')dE'}{(E-E')},$$

Thus,

$$J_v(E) = J_{HF}(E) + dJ_{vo}(E) + dJ_s(E). \qquad \text{(IV-6)}$$

It is assumed that the volume imaginary potential and the Hartree-Fock potential have the same Saxon-Woods geometries, and thus

$$J_v(E) = J_{eff}(E) + dJ_s(E), \qquad \text{(IV-7)}$$

where $J_{eff}(E) \equiv J_{HF}(E) + dJ_{vo}(E)$. In the present case, one does not have any good knowledge of the volume absorption. However, it can be shown that, with reasonable assumptions, dJ_{vo} is approximately linear with energy from -25 MeV to +25 MeV, with, by definition, a zero magnitude at the Fermi energy, E_F.[43] Thus it is not expected to contribute to the energy-dependent structure observed in J_v of the SOM. It is computationally convenient to define the quantity

$$R(E) \equiv dJ_s(E)/J_s(E), \qquad \text{(IV-8)}$$

where R(E) is the function by which the surface-imaginary potential, J_s, is multiplied to give the surface-peaked component of the real potential, dJ_s.

The R(E)-function of Eq. IV-8 was calculated from the above SOM. The calculation was based upon a simple and frequently-used approach[4,44], assuming that J_s is symmetric about the Fermi energy, E_F = -10.6 MeV. For energies $2 \cdot E_F < E < 0$, J_s was assumed to have the parabolic form $J_s = \frac{J_o}{E_F^2} \cdot (E-E_F)^2$, where J_o is the zero-energy value of the SOM (i.e., J_w of Table IV-1 at $E \equiv 0$). For $0 < E < 24$ MeV, J_s was taken directly from Table IV-1, and then assumed to fall linearly from the 24-MeV value to zero at 60 MeV. With these assumptions, dJ_s was calculated, with the results shown in Fig. IV-4. The general energy-dependent trend of dJ_s is conventional, but E_F is a particularly large negative value and thus dJ_s is significantly negative over much of the positive-energy domain. The consequent R-function of Eq. IV-8 is shown in Fig. IV-4. The smooth energy-dependent behavior is the result of fitting the calculated mesh of values with a simple cubic expression that very well describes the calculated values, and is easy to apply. The net effect of R is to

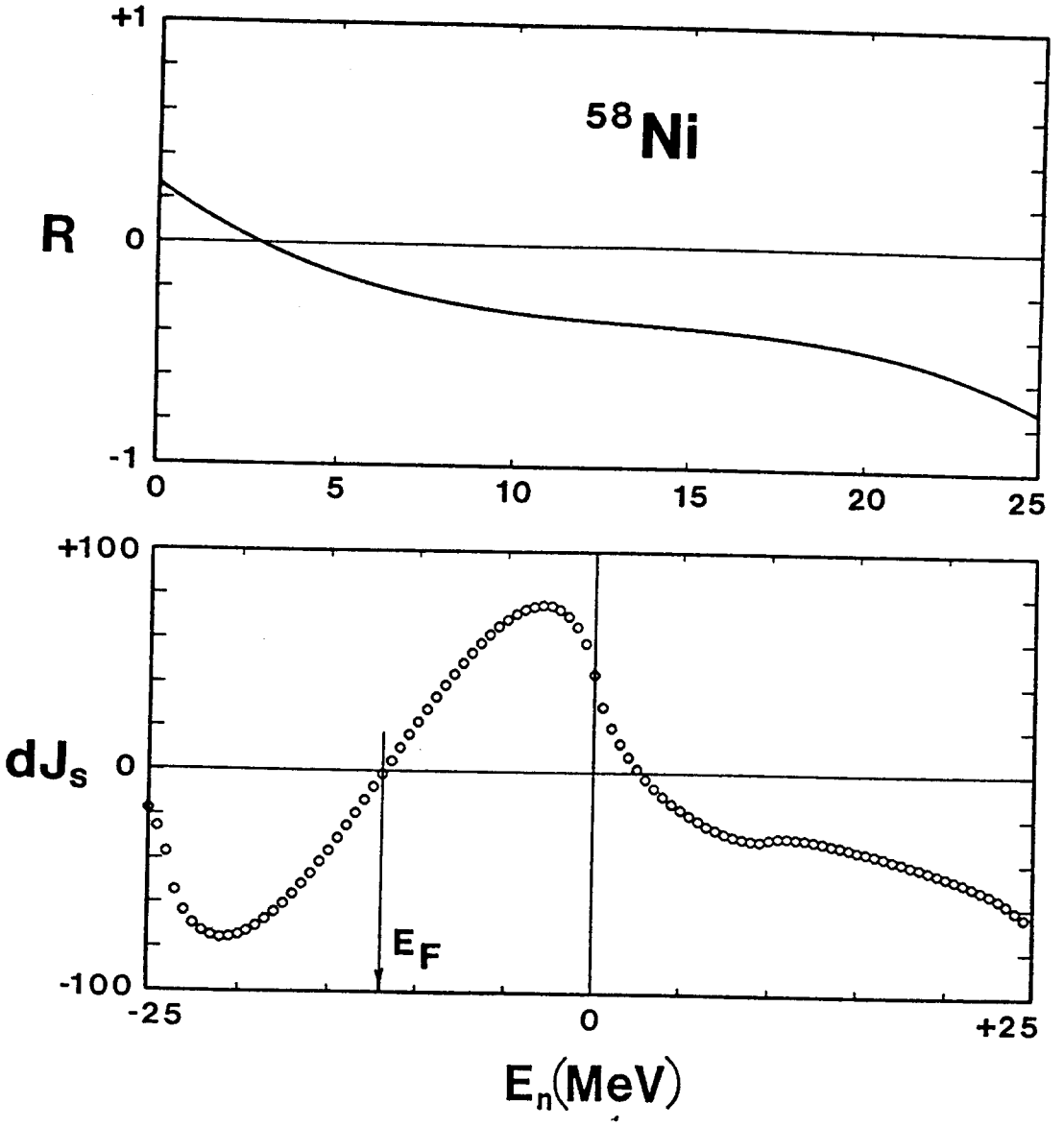

Fig. IV-4. R of Eq. IV-8 (upper), and dJ_s of Eq. IV-5 (lower) in units of MeV-fm^3.

subtract a modest surface component from J_{eff} over most of the energy range of the neutron measurements.

The chi-squares fitting was repeated using the dJ_s defined by the above R-function, and procedures identical to those outlined above for the SOM. The resulting parameters are compared with those of the SOM in Table IV-2. The SOM and DOM real-potential diffusenesses, a_v, are essentially the same. There is a similar equivalence of the real-potential radii, r_v, at low energies, but the energy dependence of the SOM r_v is significantly greater. This is not surprising as the R-function of Eq. IV-8 and Fig. IV-4 has the effect of reducing the surface portion of the real potential with energy, and thus the effective r_v increases at higher energies to maintain a description of the data base. However, it is clear that the DOM does not remove the energy dependence of r_v, and thus there are other underlying physical causes for such behavior. The imaginary diffusenesses, a_w, of the SOM and DOM are nearly identical. The imaginary radii are qualitatively similar, both generally decreasing with energy. However, the DOM does lead to a more general linear behavior of r_w as a consequence of the shape of the R-function at low energies. The energy-dependent strengths of the DOM, expressed in terms of volume-integrals-per-nucleon, are shown in Fig. IV-5. The real-potential strength, J_v, of that figure is, explicitly, the J_{eff} of Eq. IV-7, and it includes the volume-absorption contribution, dJ_{vo} of Eq. IV-5. Above $\approx$ 5 MeV, the DOM J_v decreases with energy in an approximately linear manner with a slope somewhat less than that of the corresponding quantity of the SOM (this is not surprising since J_v is proportional to r_v^3). The difference is consistent with the dJ_s of Eq. IV-5 and Fig. IV-4. Below $\approx$ 5 MeV, the J_v of the DOM displays the same type of dip about 4 MeV evident in the SOM interpretation (see Fig. IV-1). Thus, use of the DOM did not remove this artifact. Further considerations of the volume-absorption portion of the dispersion integral, dJ_{vo} of Eq. IV-5, will not alter this conclusion unless the volume absorption has a very unconventional energy dependence. The character of the imaginary strengths, J_w, of the SOM and DOM are qualitatively similar; i.e. both decease with energy in a physically-unexpected manner. J_w of the DOM lends itself to a parabolic energy parameterization, rather than the two linear segments used to parameterize J_w of the SOM, but the differences are not large and not clearly distinguished by the data.

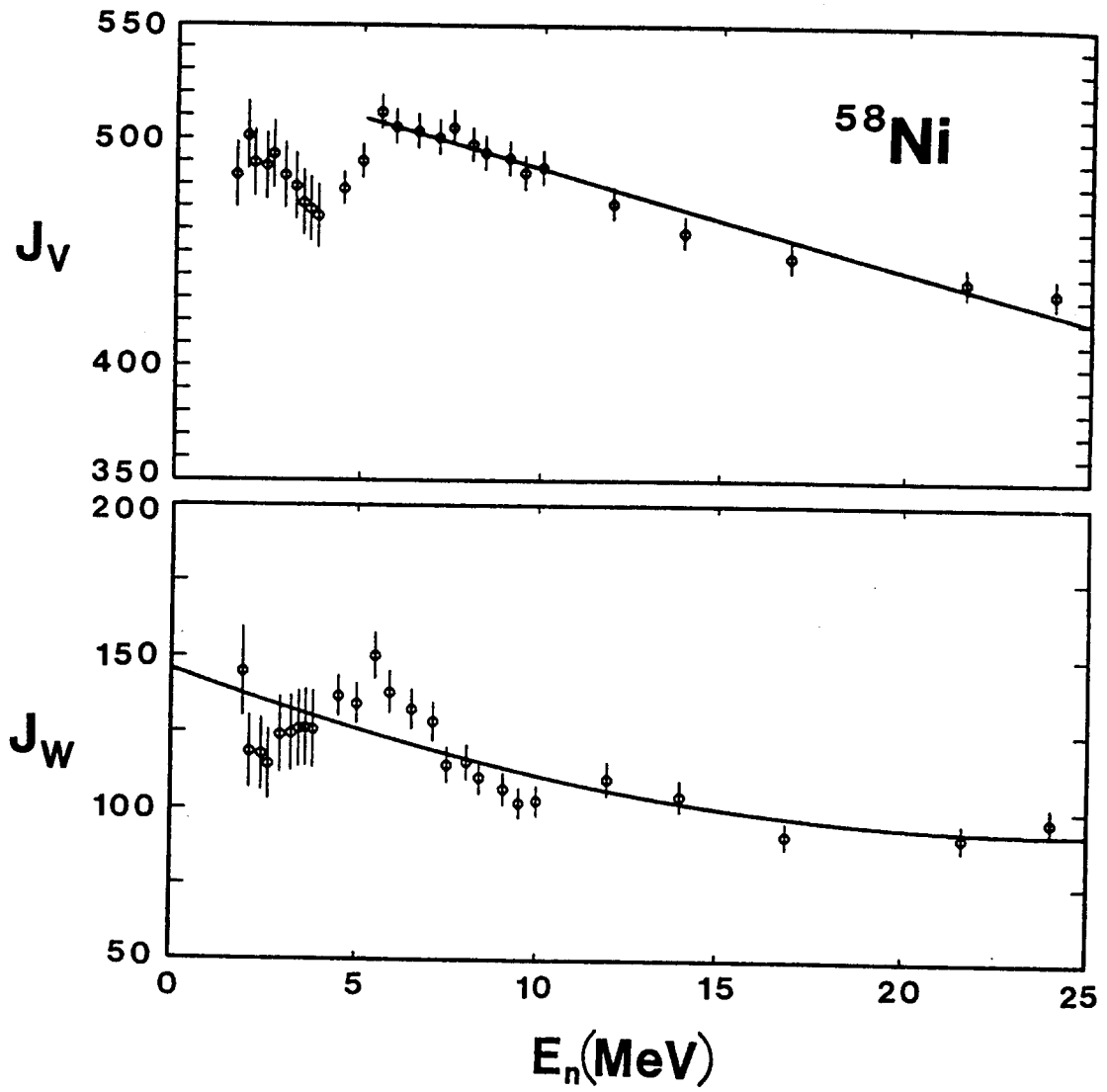

Fig. IV-5. Real (J_v) and imaginary (J_w) DOM potential strengths expressed as volume-integrals-per-nucleon (in units of MeV-fm^3). Symbols indicate the results of the individual fitting procedures, and curves the expressions given in Table IV-2. J_v corresponds to J_{eff} of Eq. IV-7.

Table IV-2. Comparison of SOM and DOM parameters. Energies, E, are in MeV.

	SOM	DOM
a_v	= 0.6461 fm	= 0.6380 fm
r_v	= (1.305 - 0.006·E) fm	= (1.315 - 0.0039·E) fm
J_v [a]	= (512.0 - 6.02·E) MeV-fm^3	= (531.0 - 4.46·E) MeV-fm^3
a_w	= (0.26 + 0.02·E) fm	= (0.25 + 0.02·E) fm
r_w	= (1.50 - 0.07·E) fm (E<4.7) = (1.16 + 0.002·E) fm (E>4.7)	= (1.327 - 0.0054·E) fm
J_w	= (133.0 - 3.9·E) MeV-fm^3 (E<10) = 94.0 MeV-fm^3 (E>10)	= (142.0 - 4.39·E + 0.0904·E^2) MeV-fm^3

a. General linear trend as per the text. For the DOM $J_v \equiv J_{eff}$ of Eq. IV-7.

The strength functions calculated with the DOM are $s_0 = 2.43 \times 10^{-4}$ and $s_1 = 0.84 \times 10^{-4}$, which are similar to the results obtained with the SOM and as deduced from resonance measurements, cited above. The neutron total and elastic-scattering cross sections calculated with the DOM are very similar to those obtained with the SOM (see Figs. IV-3 and IV-2, respectively). Thus, from the neutron scattering used in the present interpretations, there was no clear preference for either the SOM or DOM representations. Both give very similar results. In particular, there was little, if any, evidence for the "Fermi Surface Anomaly" at positive energies. Both models used here are spherical, and there is reasonable indication that, in this particular case, a collective vibrational target is involved. This matter is dealt with in the following section.

D. Phenomenological Collective Models

D-1. Vibrational Models.

As an initial premise, it is assumed in this Section that ^{58}Ni is a vibrational nucleus with a one-phonon (2^+, 1.454 MeV) first-excited state.[28] The vibrational-model interpretation coupled the ground state and this one-phonon vibrational state, using the coupled-channels calculational code ANLECIS[45], with the same potential forms used in the SOM derivation. The compound-nucleus processes were treated in a manner analogous to that described above, using deformed transmission coefficients to excitation energies of $\approx$ 3 MeV, and the transmission coefficients of the SOM at higher excitation energies. The model parameters were determined by explicitly chi-squares fitting the elastic-scattering data base, following the same procedures as outlined above for the SOM. In addition, the fitting was pursued in an iterative manner, varying the quadrupole deformation parameter, β_2, to optimize the description of the angle-integrated inelastic-scattering cross section shown in Fig. III-7. The elastic-scattering cross section is not particularly sensitive to β_2, but the inelastic-scattering cross sections of the 1.454 MeV level are (The latter were numerically derived from the differential experimental values as outlined above). The latter are know to $\approx$ 10 - 15%, implying a knowledge of β_2 to $\approx$ 8%. The resulting value of β_2 was $0.20 \pm \approx 0.015$. This value is somewhat larger than reported from coulomb-excitation measurements[46], and slightly smaller than indicated by proton-scattering measurements[47], as expected from theoretical predictions.[12] The fitting assumed a Thomas spin-orbit potential with the parameters

$$V_{so} = 6.5 - 0.035 \cdot E(\text{MeV})$$
$$r_{so} = 1.017 \text{ fm} \qquad \text{(IV-9)}$$
$$a_{so} = 0.6 \text{ fm}.$$

This is the potential of ref. 8, largely determined from polarization measurements. The potential values are somewhat different from the energy-independent formulation used for the SOM (see Eq. IV-1), but, as noted above, use of the parameters of Eq. IV-9 did not significantly alter the SOM interpretation. The resulting vibrational-model parameters are given in Table IV-3.

Comparison of Tables IV-1 and IV-3 shows that the real-potential geometries of the SOM and the one-phonon vibrational model are essentially equivalent. Any differences are probably not significant. The general real strengths, J_v, are also very similar. However, the structure in the J_v of the SOM, centered about 4 MeV, was considerably mitigated in the one-phonon interpretation, as is evident from a comparison of the relevant portions of Figs. IV-1 and IV-6 (in the latter figure all the experimentally-deduced values were used in the determination of J_v, while in Fig. IV-1 the values in the pronounced minimum were ignored). The imaginary strengths, J_w, of the SOM and one-phonon vibrational model are different (particularly at lower energies), as is evident from comparisons of Tables IV-1 and IV-3 and Figs. IV-1 and IV-6. Generally, the J_w of the one-phonon model is smaller than that of the SOM throughout the energy range of the interpretation, and the magnitude tends to slightly increase with energy. This is in marked contrast to the SOM behavior shown in Fig. IV-1, and more consistent with what one would physically expect. The coupling scheme has a pronounced impact on the absorption potential.

The neutron total cross section calculated with the one-phonon model is compared with the energy-averaged experimental data in Fig. IV-7. The agreement is reasonably good, and the calculated result is very similar to that obtained with the SOM, illustrated in Fig. IV-3. The calculated strength functions are qualitatively similar to those obtained from resonance measurements[29], and with the predictions of the SOM (e. g., $s_o = 2.07 \times 10^{-4}$ compared to the $(2.8 \pm 0.6) \times 10^{-4}$ deduced from resonance measurements, and 2.34×10^{-4} obtained with the SOM). The one-phonon vibrational model gives a good description of the elastic-scattering data from which it was developed, as illustrated in Fig. IV-8. The model also provides an acceptable description of the differential cross sections for the excitation of the first 1.454 MeV (2^+) level, as illustrated in Fig. IV-9 (and with more detail at lower energies, in Fig. III-5). The agreement is less suitable at 12 and 14 MeV, but that data came from other sources[8], and

Table IV-3. Parameters of the ^{58}Ni one-phonon vibrational model deduced by chi-squares fitting the elastic-scattering distributions.[a] Incident-neutron energy, E, is in MeV.

Real Potential

$$a_V = 0.6331 \text{ fm}$$
$$r_V = (1.3089 - 0.00638 \cdot E) \text{ fm}$$
$$J_V{}^{b} = (500.8 - 5.4 \cdot E) \text{ MeV-fm}^3$$

Imaginary Potential

$$a_W = (0.1117 + 0.05941 \cdot E - 0.001183 \cdot E^2) \text{ fm}$$
$$r_W = (1.588 - 0.0740 \cdot E) \text{ fm} \quad (E \leq 5.6)$$
$$= (1.167 + 0.0011 \cdot E) \text{ fm} \quad (E > 5.6)$$
$$J_W = (83.7 - 0.353 \cdot E + 0.02064 \cdot E^2) \text{ MeV-fm}^3$$

a. $\beta_2 = 0.20$

b. General linear trend as per the text.

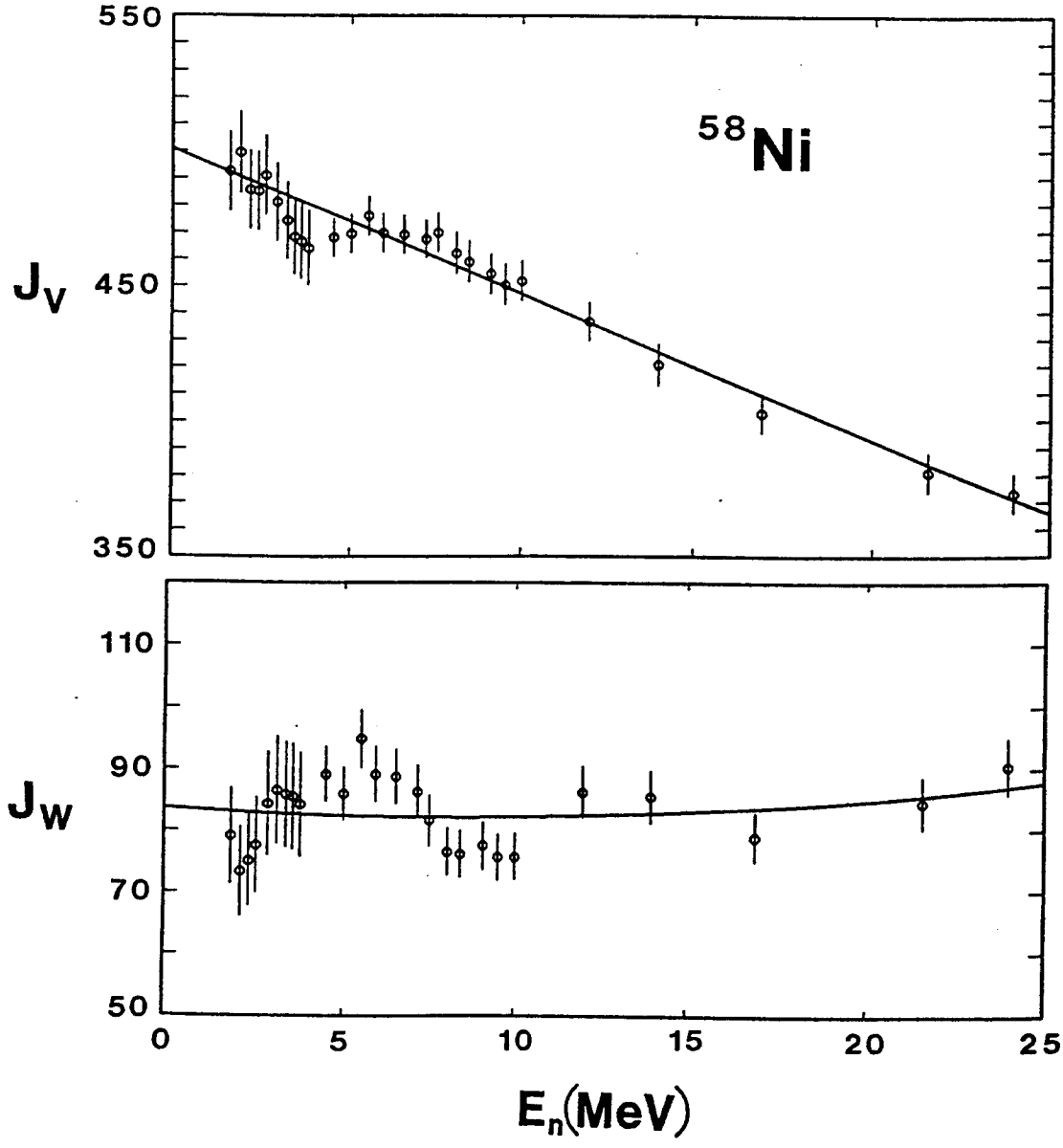

Fig. IV-6. Energy dependencies of real (J_v) and imaginary (J_w) potential strengths of the one-phonon vibrational model expressed as volume-integrals-per-nucleon, in units of MeV-fm^3.

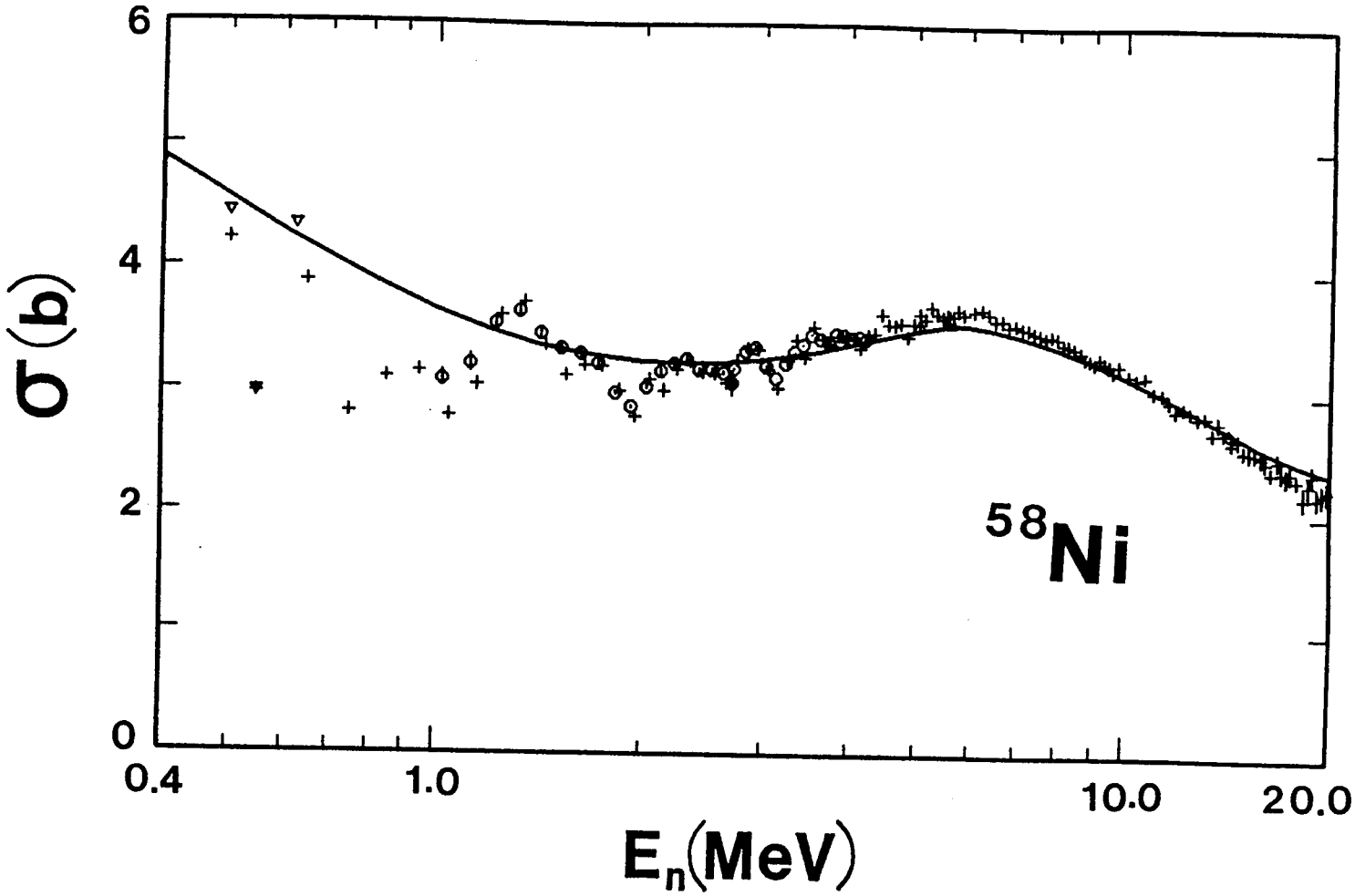

Fig. IV-7. Comparison of measured energy-averaged (symbols) and calculated (curve) neutron total cross sections. The calculations used the general one-phonon model of Table IV-3.

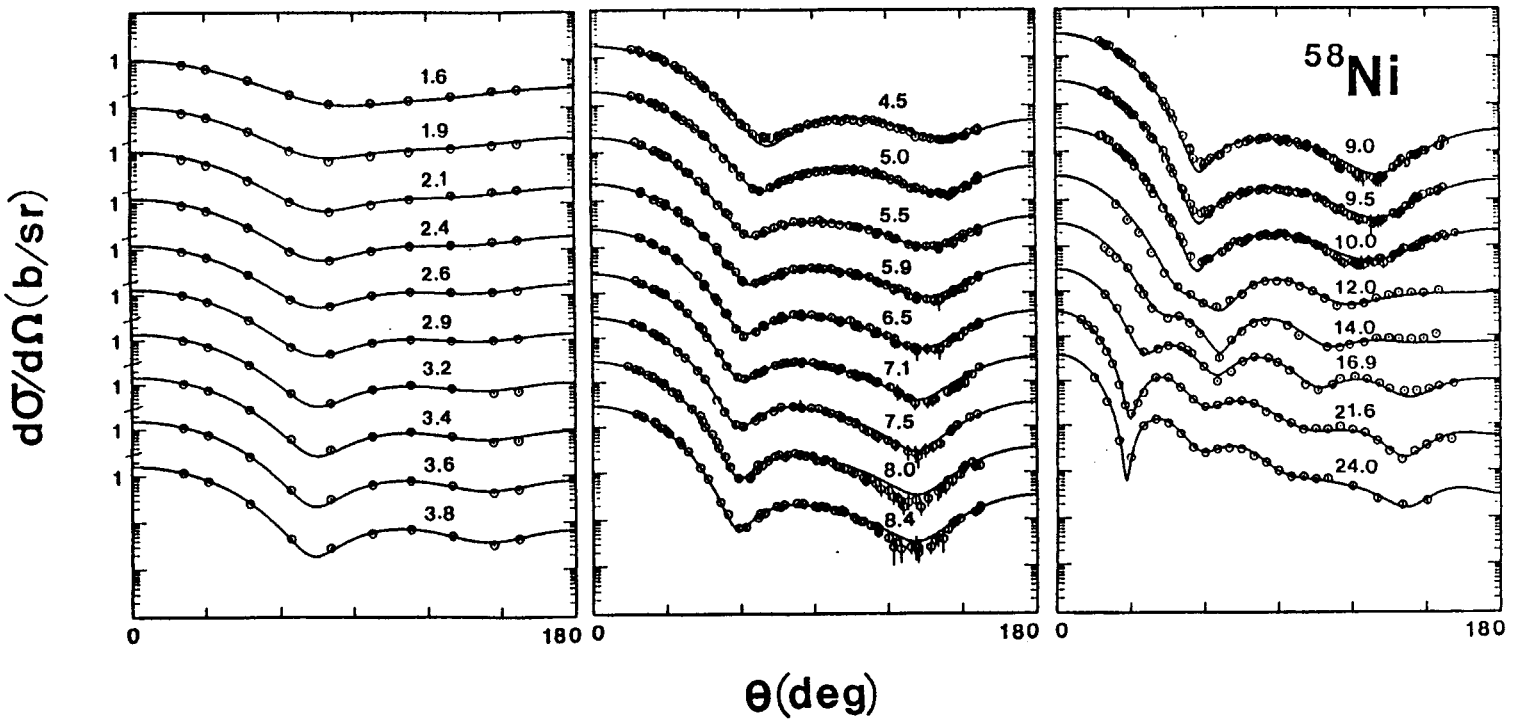

Fig. IV-8. Comparison of measured (symbols) and calculated (curves) differential elastic-scattering cross sections of ^{58}Ni. The calculations employed the one-phonon model of Table IV-3. Neutron energies are given in the respective portions of the figure, and the data are in the laboratory coordinate system.

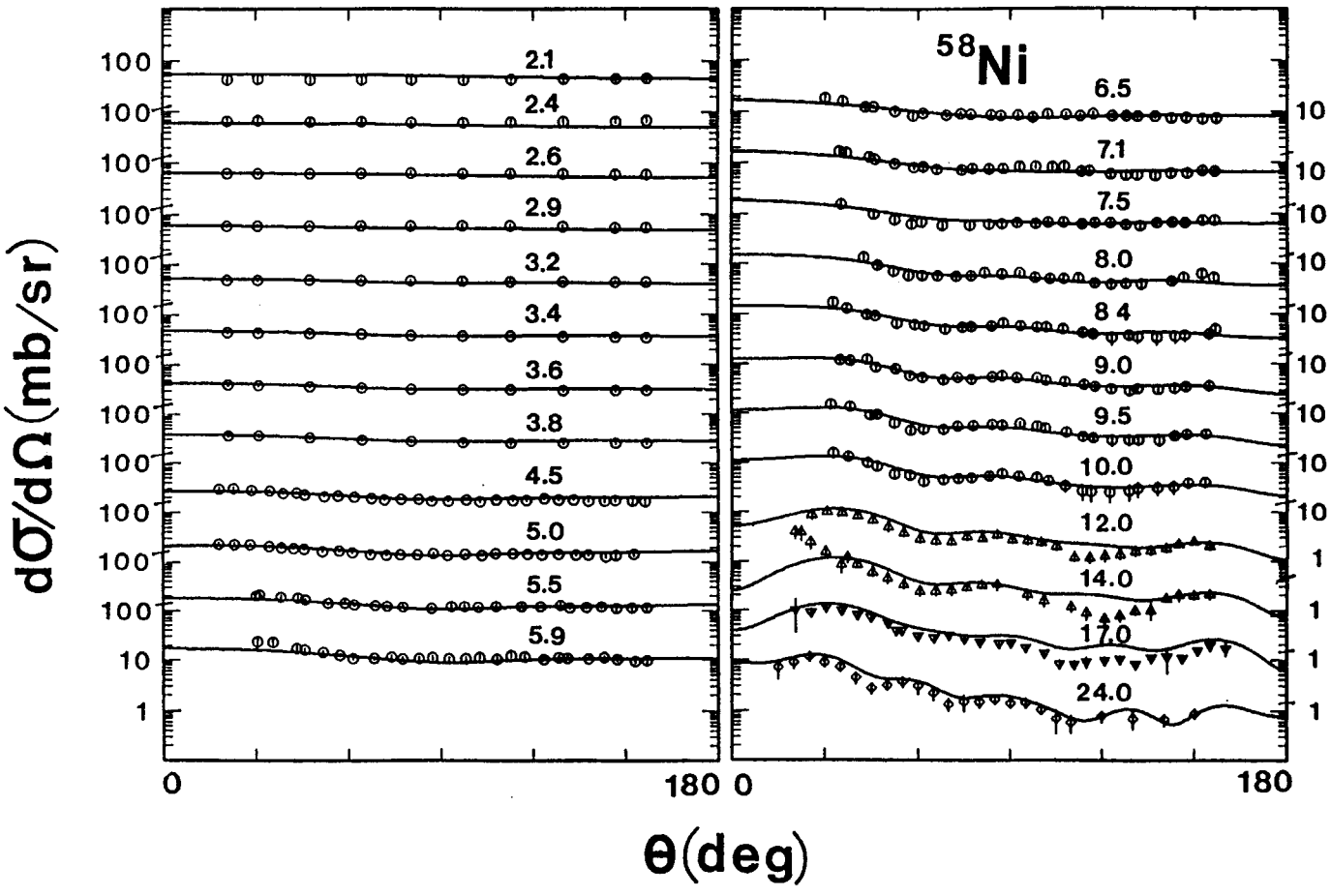

Fig. IV-9. Comparison of measured and calculated differential cross sections for the inelastic excitation of the 1.454 MeV state. Curves indicate the results obtained with the one-phonon vibrational model. "□" symbols indicate experimental results obtained at this laboratory, "Δ" results of ref. 8, "▽" results of ref. 10, and "○" the results of ref. 9. The data are in the laboratory coordinate system.

the authors had the same type of discrepancies between measured and calculated results. The comparisons are somewhat better at 17 MeV, and are quite acceptable at 21.6 and 24 MeV. The corresponding angle-integrated inelastic-scattering cross sections are also reasonably well described from threshold to 24 MeV, as shown in Fig. III-7. Perhaps the calculated angle-integrated values are slightly smaller than the measured quantities near the maximum at ≈ 2.8 MeV, but in this energy region (where targets are near the peak of the s-wave strength function) the calculated results can be quite sensitive to the exact nature of the compound-nucleus width fluctuation and correlation corrections, which may deviate slightly from the general formulation of ref. 33 used in the present calculations. Above 10 MeV, the calculated angle-integrated inelastic-scattering cross sections may be slightly larger than those deduced from measurements reported in the literature. However, definition of the latter is not sufficient to provide precise angle-integrated values via Legendre fitting, as outline above. The angle-integrated inelastic-scattering calculations, at energies of ≈ 3.8 to 8 MeV, are sensitive to the temperature of the statistical-level formalism of ref. 34 used in the present model calculations. This sensitivity was examined in an iterative manner by refitting the data base, using various temperatures, and comparing the resulting calculated angle-integrated inelastic-scattering cross sections with the experimental values. The results of these procedures supported the 1.59 MeV temperature of ref. 34. Throughout this work, the neutron polarizations were not considered in determining model parameters. However, it is interesting to compare the polarizations predicted by the one-phonon model with those observed, as reported in refs. 8 and 10. Such a comparison is given in Fig. IV-10. The calculated results are qualitatively similar to those obtained with the model largely based upon polarization considerations.[8,10] In this illustrative case, the present calculated results are superior to those of the references at the first minimum near 55^{o}, somewhat less suitable at larger angles, and none of the models properly represents the sharp minimum in the polarizations near 145^{o}. Small adjustments of the spin-orbit potential, or perhaps the introduction of an imaginary spin-orbit potential, might improve the description of the polarizations. However, such "fine tuning" of the spin-orbit potential was beyond the scope of the present interpretations, and the present model does reasonably well.

A comparison of Figs. IV-1 and IV-6 shows that the introduction of vibrational coupling in the one-phonon model alleviates the energy-dependent structure evident in the strength of the real potential in the SOM interpretation. Furthermore, Fig. III-9 indicates that there is a significant direct inelastic excitation of the second and higher excited levels, as the experimental results appreciably exceed in magnitude the predictions of compound-nucleus calculations alone. This suggests that the coupling scheme is more complex than that of the simple one-phonon model used above. That possibility was examined, assuming that ^{58}Ni is a vibrational nucleus

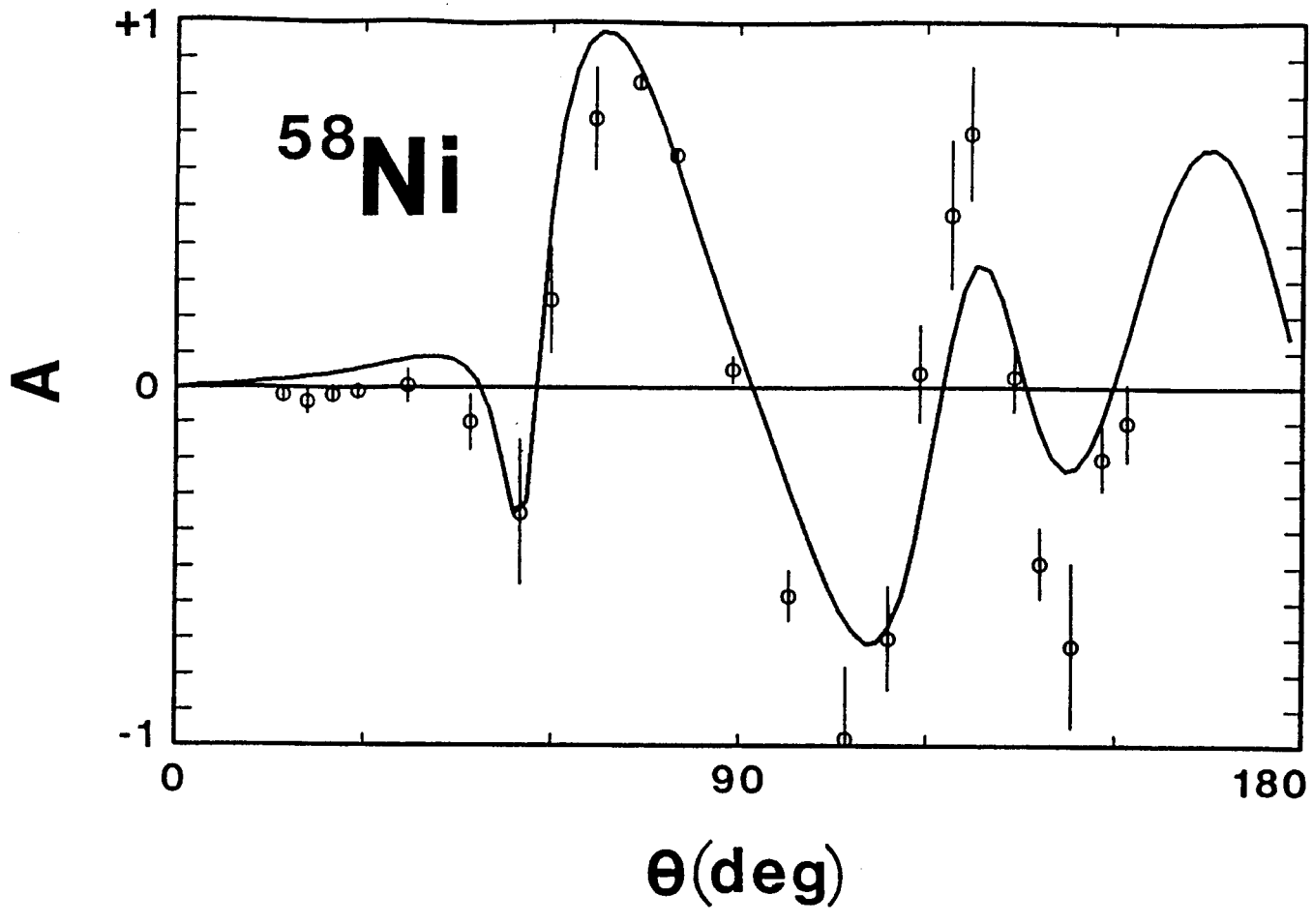

Fig. IV-10. Comparison of measured (symbols) and calculated (curve) elastic-scattering polarization at 10 MeV. The measured values are taken from refs. 8 and 10, and the calculations employed the one-phonon model of Table IV-3. The data are in the laboratory coordinate system.

with one-phonon (2^+, 1.454 MeV) and two-phonon (4^+ 2.459 MeV, 2^+ 2.776 MeV, and 0^+, 2.942 MeV) excited states. The assumption is clearly an approximation, at best, as ^{58}Ni is not a simple one- and two-phonon vibrator. However, the approximation is a reasonable vehicle for examining the effect of a more complex vibrational coupling scheme. With the one- and two-phonon assumption, the entire fitting procedure used for the one-phonon approach was repeated. The resulting model parameters are given in Table IV-4.

The one- and two-phonon model, with the potential of Table IV-4, provided a description of the total cross section, the elastic scattering, and the strength functions, which is very similar to that provided by the one-phonon model. However, in order to achieve a reasonable agreement with the angle-integrated cross sections for the excitation of the first 2^+ (1.454 MeV) level at higher energies, β_2 had to be increased to $\approx$ 0.235, following an iterative procedure similar to that outlined above for the one-phonon model. That is a value larger than obtained from proton measurements and their interpretation.[47] As pointed out above, there are uncertainties in the deduction of angle-integrated inelastic-scattering cross sections from differential experimental values by Legendre polynomial fitting, and these may systematically distort the resulting angle-integrated results. However, the fitting does indicate that the β_2 obtained with the one- and two-phonon model is significantly larger than that for the one-phonon model. The coupling of the two-phonon levels did lead to a small direct-reaction cross section at higher energies for the inelastic excitation of second, third and fourth levels, but not of a magnitude that would account for the differences between measured values and compound-nucleus calculations, as illustrated in Fig. III-9. The real potential geometries and general strengths given in Table IV-4 are similar to those obtained with the one-phonon model (Table IV-3). In particular, the energy-dependent structure in J_v, evident in the SOM interpretation, was not reduced further from that obtained in the one-phonon model. The J_w of Table IV-4 is somewhat smaller than that of Table IV-3, as is expected since more inelastic channels are now explicitly included in the fitting. Generally, the one- and two-phonon model did not improve significantly the interpretation over that achieved with the much simpler one-phonon model, and it had the detriment of considerably more calculational complexity. Thus, the one- and two-phonon model was not a particularly attractive alternative to the simpler one-phonon concept. This conclusion does not negate the importance of complex, but uncertain, coupling schemes in the interpretation of the fast-neutron interaction with ^{58}Ni. Another alternative is examined below.

Table IV-4. Parameters of the ^{58}Ni one- and two-phonon model deduced by chi-squares fitting the elastic-scattering distributions.[a] Incident neutron energy, E, is in MeV.

Real Potential

$$a_v = 0.6531 \quad \text{fm}$$
$$r_v = (1.305 - 0.0064 \cdot E) \quad \text{fm}$$
$$J_v^{b} = (508.0 - 5.75 \cdot E) \quad \text{MeV-fm}^3$$

Imaginary Potential

$$a_w = (0.290 + 0.0183 \cdot E) \quad \text{fm}$$
$$r_w = (1.500 - 0.0547 \cdot E) \quad \text{fm} \quad (E \leq 5.6)$$
$$= 1.175 + 0.0033 \cdot E \ ) \quad \text{fm} \quad (E > 5.6)$$
$$J_w = (77.9 + 0.131 \cdot E) \quad \text{MeV-fm}^3$$

a. $\beta_2 = 0.235$

b. General linear trend.

D-2. Rotational Model

It is clear, from the remarks above, that the fast-neutron interaction with ^{58}Ni involves collective phenomena. Major aspects of the processes are described by a relatively simple vibrational model. However, that approach has shortcomings, notably residual energy-dependent structure in the real-potential strength. More complex, and unknown, couplings could be contributing factors. As an extreme alternative, a collective rotational model was examined. Though ^{58}Ni is not a simple rotor, rotational (or any very strong) coupling can lead to a significant reorientation effect which appreciably changes the neutron elastic scattering.[5,7] A simple rotational model was assumed consisting of a 0^+ g.s., coupled to 1.454 MeV (2^+) and 2.459 MeV (4^+) excited levels, with $\beta_2 = 0.20$ and $\beta_4 = 0.05$. The corresponding potential was then determined by chi-squares fitting the elastic scattering data in the same manner as described above, with the spin-orbit potential of Eq. IV-9. The resulting potential parameters are given in Table IV-5, and the energy dependencies of the real and imaginary-potential strengths are shown in Fig. IV-11.

A comparison of Tables IV-3, -4 and -5 shows that the real potentials of the vibrational and rotational models are similar. The diffusenesses are nearly identical and, while the real radius and strength of the rotational model are somewhat larger at zero energy, the increase is compensated by larger energy-dependent slopes. Likewise, the imaginary vibrational and rotational potentials do not differ by a great deal. The differences in r_w and a_w are probably within the uncertainties of the parameterizations. The imaginary strengths are consistent (to within $\approx$ 10%) over the 1.0 to 20.0 MeV range of the interpretation. The fact that J_w of the rotational model is energy independent while that of the vibrational model has a very weak quadratic energy dependence is probably of no significance, as illustrated by a comparison of Figs. IV-6 and IV-11. Both the rotational and vibrational models display similar energy-dependent structure in the real-potential strength near 4 MeV, thus a radical change in the coupling scheme did nothing to alleviate this problem.

The rotational model gave essentially the same phenomenological results as the vibrational model. The calculated total cross sections to 20 MeV are very similar. In both cases, calculated elastic- and inelastic-scattering cross sections were consistent with the experimental data base and with one another. Strength functions were in qualitative agreement (e.g., $s_0 = 2.64 \times 10^{-4}$ for the rotational model). Thus, when using an entirely different (and probably

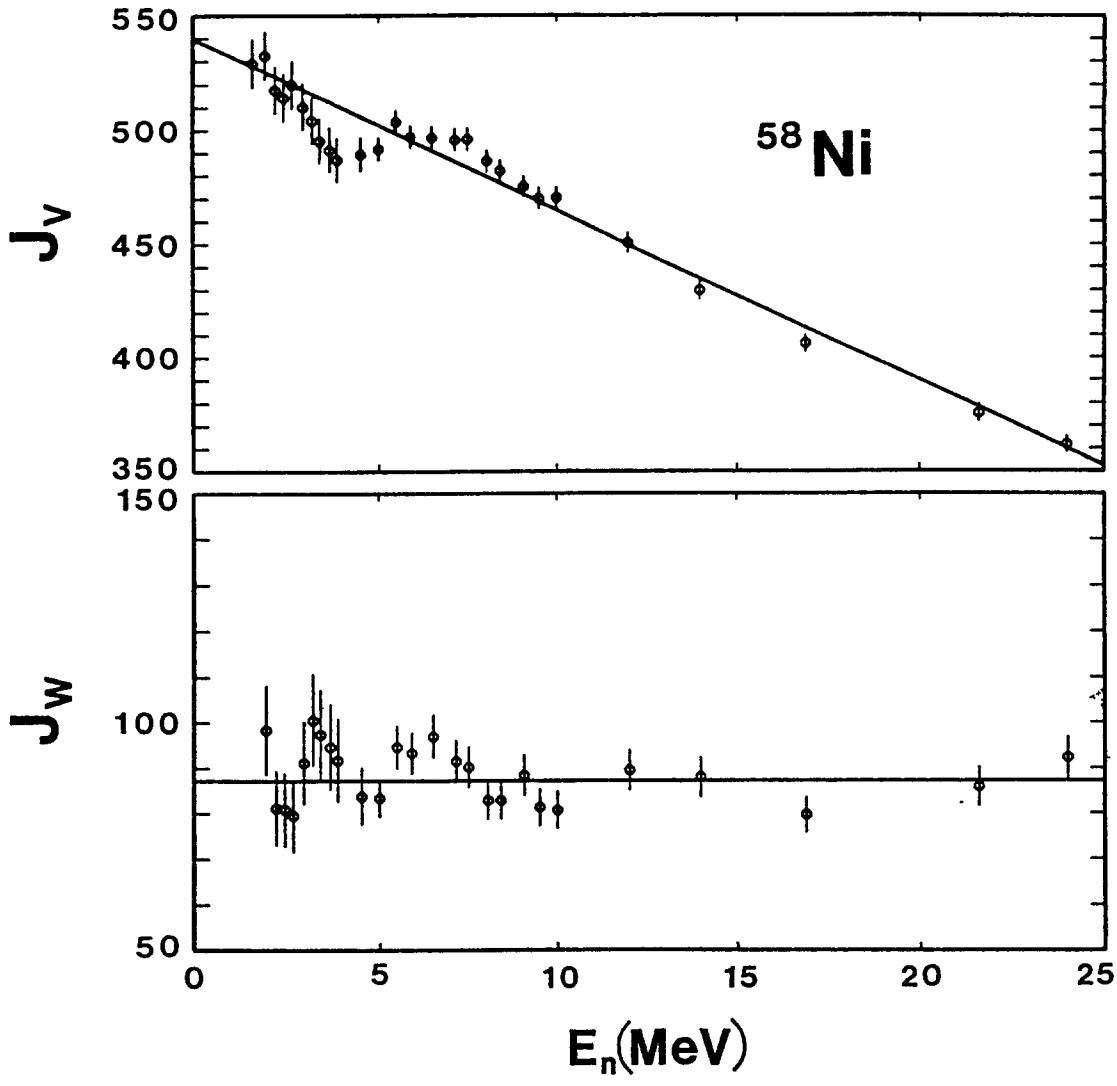

Fig. IV-11. Energy dependencies of the real (J_V) and imaginary (J_W) potential strengths of the rotational model expressed as volume-integrals-per-nucleon, in units of MeV-fm^3.

Table IV-5. Parameters of the ^{58}Ni rotational model deduced by chi-squares fitting the elastic-scattering distributions.[a] Incident energies, E, are given in MeV.

Real Potential

$$a_v = 0.6353 \text{ fm}$$
$$r_v = (1.3524 - 0.0102 \cdot E) \text{ fm}$$
$$J_v{}^{b} = (539.6 - 7.479 \cdot E) \text{ MeV-fm}^3$$

Imaginary Potential

$$a_w = (0.03821 + 0.0436 \cdot E - 0.000484 \cdot E^2) \text{ fm}$$
$$r_w = (1.508 - 0.0464 \cdot E) \text{ fm} \quad (E \leq 6.15)$$
$$= 1.222 \text{ fm} \quad (E > 6.15)$$
$$J_w = 87.1 \text{ MeV-fm}^3$$

a. $\beta_2 = 0.20$ and $\beta_4 = 0.05$. The spin-orbit potential is that of Eq. IV-9.
b. General linear trend as per the text.

inappropriate) rotational model, the results are similar to those obtained with the vibrational model; and have similar shortcomings.

V. SUMMARY DISCUSSION

One would hope that the real potential is least sensitive to specific nuclear-structure effects, and therefore is of a more "global" nature. The ^{58}Ni real potentials obtained using SOM, DOM, vibrational and rotational models are collected in Table V-1 for ease of comparison.

It is evident that the real diffusenesses, a_v, resulting from the various interpretations are essentially identical. Furthermore, the values are in very good agreement with that obtained from the ^{59}Co SOM interpretation (0.6355 fm) of ref. 37, the ^{58}Ni interpretation (0.656 fm) of ref 8, and generally consistent with the values obtained in investigations over a wide mass region and as given by "regional" and "global" neutron models.[40,41,43,48-53] Thus the real diffuseness appears to be essentially a constant global parameter, not particularly sensitive to the details of the model used.

The real-potential radii, r_v, are essentially identical for the SOM and vibrational models, and both decrease significantly with energy. The r_v of the DOM is similar, but with less energy dependence, as one would expect from the R-function of Eq. IV-8, shown in Fig. IV-4. Consideration of the dispersion relation mitigated the energy dependence of the SOM r_v by $\approx$ 30%, but did not remove it. There must be other underlying causes for such a behavior.

It is convenient to compare potentials at incident-neutron energies of $\approx$ 8 MeV, which is a high enough energy to avoid the complexities of compound-nucleus process (and still have an interpretation relatively sensitive to nuclear structure) and the R-function of Eq. IV-8 is approximately zero at that energy. The latter condition is not as strictly met for ^{58}Ni due to the large negative value of the Fermi energy, but the R-function (Fig. IV-4) remains a modest negative quantity. Chiba et al.[48] have made such 8-MeV comparisons, and show that the reduced radius is mass dependent, having the form

Table V-1. Comparison of SOM, DOM, vibrational and rotational model real potentials (taken from Tables IV-1, IV-2, IV-3 and IV-5).

Model	a_v [a]	r_v [a]	J_v [b]
SOM	0.6461	1.305-0.006·E	512-6.02·E
DOM	0.6380	1.315-0.004·E	531-4.46·E
Vib.[c]	0.6331	1.309-0.006·E	501-5.40·E
Rot.	0.6353	1.352-0.010·E	540-7.48·E

a. in fms.
b. in MeV-fm^3.
c. one-phonon model.

$$r_v = r_0 + r_1/A^{1/3}$$
$$r_0 = 1.1476 \text{ fm} \qquad (V\text{-}1)$$
$$r_1 = 0.4416 \text{ fm},$$

where A is the target mass number. The predicted r_v for ^{58}Ni is 1.2617 fm at 8 MeV, compared to the values of 1.2570 fm and 1.2579 fm obtained in the SOM and vibrational interpretations, respectively. ^{59}Co studies[37] led to a SOM radius of 1.2624 MeV at 8 MeV, consistent with the present ^{58}Ni results and the systematic predictions of Eq. V-1. Thus it seems that Eq. V-1 is a reasonable "global" representation of r_v at 8 MeV. At other energies, variations in the Fermi energy, and thus in the R-function, will make some differences in the energy dependence and zero-energy intercept of r_v, but only by modest amounts. Intercepts are generally in the range 1.30 to 1.35 fm and slopes -0.005 to -0.010 per MeV up to 20 MeV when r_v is given a linear representation, and this representation is probably a reasonable "global" estimate. Clearly, the above remarks do not imply energy dependencies that extend indefinitely, and there must be an asymptotic approach to constant r_v values above $\approx$ 20 MeV if there are not to be serious consequences. That asymptotic value appears to be $\approx$ 1.2 fm, which is qualitatively consistent with the commonly encountered proton SOM r_v values, and with the above linear representation and constants. Numerical approximations for this asymptotic behavior have been suggested; for example, by Delaroche et al.[53] The rotational model r_v values are not as consistent with the above remarks, but that model involves a coupling scheme that is probably far from physical reality.

For the moment, we ignore the structure in the real-potential strength, J_v, and consider only general magnitude and energy-dependent trends. The J_v of the SOM and vibrational model are very similar in both intercept and energy dependence. The larger intercept and lesser slope of the J_v obtained from the DOM is a reflection of the significantly smaller slope of the DOM r_v (as J_v is proportional to r_v^3) and the energy-dependent shape of the R-function shown in Fig. IV-4. Chiba et al.[48] have pointed out that the systematics of J_v at 8 MeV are given by

$$J_v = K \cdot \left[1 - \xi \cdot (N-Z)/A\right] \cdot (r_0 + r_1/A^{1/3})^3, \qquad (V\text{-}2)$$

where r_0 and r_1 have the values of Eq. V-1, A is the mass number, N and Z the neutron and proton number respectively, K = 234.2 MeV and ξ = 0.53. Expressed in this form, the parameter is consistent with the nucleon-nucleon scattering data[54] and (p,n)-reaction results.[55] The systematics of J_v implied by Eq. V-2 are reasonably well supported by a number of SOM interpretations.[4,37,43,56-58] One can generalize Eq. V-2 to other energies, assuming the energy dependence of the radius is in r_0, and that the isovector constant, ξ, is energy independent. Then Eq. V-2 can be expressed in the energy dependent form

$$J_v(E) = (K_0 + K_1 \cdot E + K_2 \cdot E^2) \cdot \left[1 - 0.53 \cdot (N-Z)/A\right] \cdot (r_0 + a \cdot E + 0.4416/A^{1/3})^3. \quad \text{(V-3)}$$

Using the ^{58}Ni parameters following from the SOM (r_0 = 1.1909, a = -0.006 and $J_v(E)$ of Table IV-1), it is found that K_0 = 233.5, K_1 = 0.5143 and K_2 = -0.01331. The results obtained with Eq. V-3 are very similar to the MeV values deduced by Chiba et al.[48] (i.e., to within $\approx$ 1% or better). However, these particular parameters depend upon the energy dependence of r_v (i.e., on a, with the above assumptions), and that is partly related to the particular nuclear structure through the dispersion relationship of Eq. IV-3. Moreover, the SOM is dependent upon the Fermi energy, which will vary from target to target. Thus, the concept of a "global" SOM real-potential strength has fundamental shortcomings. However, the DOM J_{eff} of Eq. IV-7 is probably a relatively good "global" quantity consisting of the Hartree-Fock component and a small dispersion contribution from volume absorption.

The above discussion has ignored the structure in the real-potential strength centered about 4 MeV, as illustrated in Figs. IV-1, -5, -6 and -11. It is a prominent feature in SOM and DOM interpretations. This structure is appreciably mitigated by the introduction of vibrational coupling, and it has been shown that the use of a simple SOM in the interpretation of collective nuclei can lead to structure in the real-potential strength which is qualitatively similar to that evident, for example, in the above SOM interpretation.[13] The fact that the structure was not completely removed in the one-phonon vibrational interpretation probably reflects more complex couplings that were not taken into account in this simplified concept. The situation was not further improved by including two-phonon levels in the vibrational model, nor by the consideration of an entirely different, and probably inappropriate, rotational model. More complex coupling schemes may be a significant

factor in producing the observed structure in the real-potential strength, but their detailed nature remains unclear.

The present interpretations, largely based upon elastic-scattering data, are not sensitive to modest variations in the spin-orbit potential, but the resulting overall models gave descriptions of polarization results reported in the literature comparable to those obtained with models specifically developed for that purpose.[8] The present experimental elastic-scattering results, and those generally available in the literature, do not extend to very large scattering angles (e.g., approaching 180^{o}) where the effects of the spin-orbit potential can be significant.

The imaginary potential is expected to be sensitive to the particular target, and also to reflect collective effects. The ^{58}Ni imaginary potentials deduced from the present work are summarized in Table V-2. In all the above cases the imaginary diffuseness, a_w, is very narrow at zero energy, and increases with energy to values in the range $\approx$ 0.6 - 0.8 fm at 20 MeV. For the SOM and DOM, a linear energy dependence appeared suitable, while for the collective models a quadratic behavior seemed more appropriate, but the qualitative behavior is the same. The zero-energy intercepts are not well defined due to fluctuations in the lower-energy data. Similar energy trends of a_w have been noted in interpretations of other neutron-scattering processes (e.g., see refs. 37, 43, 56 and 58). Qualitatively, the absorption is very narrowly concentrated at the nuclear surface at low energies, and then broadens into the nucleus as the energy increases. This is physically reasonable, and in many "global" models it is approximated with the extreme assumption of introducing energy-increasing volume absorption at $\approx$ 10 MeV with a geometry similar to the that of the real potential. As noted in Section IV, repeated investigations in the present interpretations did not support a volume-absorption term to at least 24 MeV. The energy-increasing imaginary diffuseness is probably a more realistic approximation of a trend toward absorption deepening into the nucleus with energy up to at least 25 MeV.

It has long been known that optical potentials based upon low-energy observables (e.g., the strength functions) have imaginary-potential radii larger than those of the real potential as $E \rightarrow 0$.[40] That is true of the present interpretations, and the r_w rapidly decreases with energy to $\approx$ 5 - 6 MeV where the values are significantly smaller than those of the real potential. From that point onward the r_w values are approximately constant. The exception is the DOM model. It has been shown that SOM interpretations of vibrational nuclei will result in $r_w < r_v$ [13,37], but the phenomenon

Table V-2. Comparisons of SOM, DOM, vibrational and rotational model imaginary potentials (taken from Tables IV-1, -2, -3, and -5). Incident neutron energies, E, are in MeV.

Model	a_w [a]	r_w [a]	J_w [b]
SOM	0.26+0.02·E	1.500-0.070·E (E<4.7)	133.0-3.9·E (E<10)
		1.160+0.002·E (E≥4.7)	94.0 (E≥10)
DOM	0.25+0.02·E	1.327-0.005·E	142.0-4.39·E +0.0904·E^2
Vib.[c]	0.112+0.0594·E -0.0012·E^2	1.588-0.074·E (E≤5.6)	83.7-0.353·E +0.0206·E^2
		1.167+0.001·E (E>5.6)	
Rot.	0.04+0.0436·E -0.0005·E^2	1.508-0.046·E (E≤6.2)	87.1
		1.222 (E>6.2)	

a. in fms.
b. in MeV-fm^3.
c. one-phonon model.

persists even in the present vibrational interpretations. At approximately 20 MeV, the two radii become equal and presumably remain so at higher energies. In the case of the DOM, the two radii are essentially the same throughout the energy range of the present interpretations. Moreover, the DOM r_w has a relatively linear energy dependence, with little or no evidence of low and high energy branches. This reflects the rather sharp change in the R-function of Eq. IV-8 (and Fig. IV-4) in the 0 to $\approx$ 6 MeV range. Thus, in this case and in a spherical context, consideration of the dispersion relationship alleviates the unusual behavior of r_w resulting from a simple SOM interpretation. This is not surprising as the R-function has a strong energy dependence at relatively low energies. In other instances the Fermi energy is different and the R-function will be somewhat different in shape and energy scale. It is reasonable to expect the same effect of the dispersion relationship on r_w in the collective interpretations, although that was not explicitly explored in the present work.

The imaginary-potential strengths, J_w, of the SOM and DOM models both fall with energy to about 5 - 6 MeV and then are essentially constant. This is not expected as the imaginary potential represents channels not explicitly accounted for in the calculations, and the latter should increase with energy, resulting in an increase in the imaginary strength. A similar behavior was noted in a SOM interpretation of the neutron interaction with ^{59}Co.[37] However, when either vibrational or rotational collective effects are considered, the imaginary strength is approximately constant or increases somewhat with energy, and thus is more in accord with physical expectations. Moreover, the magnitude of J_w for the vibrational interpretation is 10% - 20% smaller than the higher-energy asymptotic values obtained with the SOM of DOM, and the difference increases as the energy decreases. A spherical interpretation of a collective vibrator will over estimate the imaginary-potential strength considerably, as pointed out some time ago by Lawson et al.[39] However, the J_w values obtained with the vibrational model are still much larger than those encountered near neutron shell closures (e.g., near N = 50 and A = 90[4,37,57,59]), and similar large values of J_w have been reported from (p,n) measurements near threshold in this mass region.[60] Imaginary-potential strengths are certainly of no more than a "regional" nature; being influenced by, for example, neutron shell closures, neutron excess, etc., and generally are specific to the particular target involved.

The elastic-scattering distributions are only moderately sensitive to the value of the deformation parameter, β_2. However, the

cross sections for inelastic excitation of the 1.454 MeV (2^+) level are very much so, and they were used to constrain the values of β_2, as discussed in Section IV. A value of $\beta_2 = 0.20 \pm \approx 0.015$ was selected for the one-phonon vibrational model. This value is consistent with the predictions of Madsen et al.[12] based on microscopic effective-charge theory. Those authors predict that β_2 for (n,n') processes should lie between the electro-magnetic β_2 and that for the (p,p') process. At energies of $\approx$ 20 MeV the ^{58}Ni β_2 for (p,p') processes is 0.21[47], and the respective β_2(em) = 0.1828[46], thus the trend in β_2 values is reasonably consistent with the theoretical predictions, though the uncertainties are large.

Unfortunately, things are not quite that simple. What one should compare are deformation lengths, $\delta = R \cdot \beta_2$, and β_2 values are dependent upon the type of analysis used in their derivation (e.g., values obtained from coupled-channels and DWBA results may differ significantly). When the radii are energy dependent (as they are in this case and as is implied by the dispersion relationship) comparisons of deformation lengths are meaningful only at some reference energy. That is not easy as δ_{nn} and δ_{pp} are generally obtained from measurements at quite different energies, and the respective models must be related through the isovector term of the potential and the Coulomb correction factor, both of which are uncertain. In addition, the radii of neutron and proton models are inherently different. For the present, the comparisons are made at 24 MeV, where one might hope that the radii have asymptotically approached energy-constant values. With this assumption, and using the radius of the one-phonon vibrational model of the present work for determining δ_{nn} and δ_{pp}, one gets the value δ_{nn} = 0.8948 fm using the β_2 of the present work, δ_{pp} = 0.9470 fm using the β_2 of ref. 47, and δ_{em} = 0.8491 using the parameters of ref. 46. These values are consistent with the prediction of ref. 12 that $\delta_{em} < \delta_{nn} < \delta_{pp}$ (although the δ_{nn} and δ_{pp}uncertainties may be large). However, at 10 MeV, the present work leads to δ_{nn} = 0.9639 fm and, unless the proton-potential radius has a similar energy dependence, the conclusions are quite different. The comparison further degenerates as the energy decreases, and one enters a region where detailed knowledge of the proton potential is forbidden by the Coulomb barrier. The above problems may have contributed to differences in β_2 deduced from neutron measurements reported in the literature.[8,9]

The present one- and two-phonon vibrational interpretation suggests a β_2 significantly larger than that obtained in the one-phonon interpretation. In effect, the result of coupling the three additional two-phonon levels is some dilution of the direct-excitation of the first-excited state. It is disturbing that the introduction of two-phonon coupling did not adequately account for the relatively large higher-energy cross sections encountered for the excitation of the two-phonon levels, as illustrated in Fig. III-9. This is another indication, together with the above-cited structure in the real-potential strength, that the simple vibrational coupling schemes are only a first approximation of a more complex configuration that is not properly accounted for.

There are relatively few comparable models[8-11] for the neutron interaction with ^{58}Ni. Most of them are limited in energy scope, and thus give little insight into the energy dependencies of the parameters. Generally, the low-energy region is not addressed, and the geometries are energy independent. But this is not consistent with the dispersion relationship and, possibly, other physical properties. In view of these matters, only limited model comparisons are possible. The 24-MeV vibrational model of Yamanouti et al.[9] has geometries and strengths that are similar to those of the present vibrational model (e.g., J_v = 375.3 MeV-fm^3, compared to 371.2 MeV-fm^3 of the present work). The vibrational model of Guss et al.[8] has a much smaller ($\approx$ 7%) real-potential strength than that of the present work at a representative 10-MeV energy. The 21.6-MeV vibrational model of Olsson et al.[11] is consistent with that of the present work in both geometries and strengths. None of these models address the difficult problem of the minimum of the total cross section in the several MeV region, although Pedroni et al.[10] point out that energy dependent geometries, such as those used in the present interpretations, are probably required to describe the total cross section over a wide energy span, including the few-MeV region.

The dispersion relationship implies that a conventional SOM or coupled-channels interpretation will lead to energy-dependent parameters. However, there are probably other additional factors contributing to these energy-dependencies. In this particular case, the use of the dispersion relation seems to alleviate some of the energy-dependent features of the imaginary potential evident when dispersion effects are ignored. The potentials should smoothly extrapolate to the shell-model potential, and should provide reasonable predictions of the binding energies of bound particle and hole states. In the case of ^{58}Ni, the prominent effects of the DOM are at particularly low energies due to the large negative value of the Fermi energy, and there is essentially no evidence of the Fermi Surface Anomaly at unbound energies. The extrapolation of the

neutron-based DOM into the bound-state regime, and the associated implications, will, be dealt with in ref. 61.

This work provides the basic or applied practitioner with models that should prove very effective in calculating of the fast-neutron interaction with ^{58}Ni. For many purposes, the simple SOM will provide good results, and it serves as a basis for more extended calculations (e.g., DWBA calculations, neutron emission predictions, etc.). It has unusual properties that reflect the fundamental collective nature of the interactions. The spherical DOM alleviates some of the peculiarities of the simple SOM, particularly where associated with the imaginary potential. The one-phonon vibrational model successfully describes many aspects of the interaction of fast neutrons with ^{58}Ni, and should prove very satisfactory for most applications. However, it remains a simple approximation to a far more complex process. Its shortcomings are reflected in some unusual model parameters and an inability to describe some aspects of the process (e.g., the inelastic excitation of higher-lying levels).

Acknowledgments

The authors are very much indebted to Dr. R. D. Lawson for his continued interest in this work and his detailed guidance.

References

1. For example, the radiation resistant steel alloy HT-9.

2. R. D. Lawson, Theory of the Nuclear Shell Model Clarendon Press, Oxford (1980).

3. C. Mahaux and H. Ngo, Nucl. Phys. A378 205 (1982); Phys. Lett. 100B 285 (1981).

4. R. D. Lawson, P. T. Guenther and A. B. Smith, Phys. Rev. C36 1298 (1987).

5. R. D. Lawson, P. T. Guenther and A. B. Smith, Nucl. Phys. A519 487 (1990).

6. C. Mahaux and R. Sartor, Phys. Rev. Lett. 57 3015 (1986).

7. S. E. Hicks and M. T. McEllistrem, Nucl. Phys. A468 372 (1987).

8. P. P. Guss, R. C. Byrd, C. E. Floyd, C. R. Howell, E. Murphy, G. Tungate, R. S. Pedroni, R. L. Walter, J. P. Delaroche and T. B. Clegg, Nucl. Phys. A438, 187 (1985).

9. Y. Yamanouti, J. Rapaport, S. Grimes, V. Kulkarni, R. W. Finlay, D. Bainum, P. Grabmayr and G. Randers-Pehrson, Proc. Int. Conf. on Nucl. Cross Sections for Technology, Natl. Bur. Stds. Special Pub.-594, page 146 (1980).

10. R. S. Pedroni, C. R. Howell, G. M. Honore, H. G. Pfutzner, R. C. Byrd, R. L. Walter and J. P. Delaroche, Phys. Rev. C38, 2052 (1988).

11. N. Olsson, E. Ramstrom and B. Trostell, Nucl. Phys. A509 161 (1990).

12. V. Madsen, V. Brown and J. Anderson, Phys. Rev. C12 1205 (1975).

13. A. B. Smith, unpublished laboratory memorandum available from the author (1989).

14. C. Budtz-Jorgensen, P. Guenther, A. Smith and J. Whalen, Z. Phys. A306 265 (1982).

15. W. P. Poenitz, A. B. Smith and J. F. Whalen, Nucl. Sci. and Eng. 78 33 (1986).

16. W. P. Poenitz and J. F. Whalen, Argonne National Report, ANL/NDM-80 (1983).

17. A. Smith, P. Guenther, J. Whalen, W. McMurray, M. Renan and I. van Heerden, Z. Phys. A319 47 (1984).

18. A. Smith, P. Guenther, J. Whalen, I. van Heerden and W. McMurray, J. Phys. G11 125 (1985).

19. P. Guenther, A. Smith and J. Whalen, Phys. Rev. C12 1797 (1976).

20. D. Miller, Fast Neutron Physics Vol.-II, Editors J. Marion and J. Fowler, Interscience Publishers, New York (1963).

21. Nuclear Standards File IAEA Tech. Report 227, Editors H. Conde', A. Smith and A. Lorenz, IAEA Press, Vienna (1983).

22. A. Smith, P. Guenther, R. Larson, C. Nelson, P. Walker and J. Whalen, Nucl. Instr. and Methods 50 277 (1967).

23. A. Smith, P. Guenther and R. Sjoblum, Nucl. Instr. and Methods 140 397 (1977).

24. P. Guenther, The Scattering of Fast Neutrons from the Even Isotopes of Tungsten Thesis, University of Illinois (1977); See also, A. B. Smith, MONTE-POLY and MONTE-SPHERE Monte-Carlo correction Programs, unpublished memorandum (1988), available from the author.

25. J. A. Harvey, private communication (1986), data available from the National Nuclear Data Center, Brookhaven National Laboratory.

26. P. Boschung, J. Lindow and E. Schrader, Nucl. Phys. A161 593 (1971).

27. C. Budtz-Jorgensen, P. Guenther, A. Smith and J. Whalen, Z. Phys. A306 265 (1982).

28. L. K. Peker, Nuclear Data Sheets 42 457 (1984).

29. Neutron Cross Sections S. F. Mughabghab, M. Divadeenam and N. E. Holden, Vol.-1, part-A, Academic Press, New York (1981).

30. A. B. Smith et al., An Evaluated Neutronic File for ^{58}Ni, to be published.

31. P. E. Hodgson, Nuclear Reactions and Nuclear Structure Clarendon Press, Oxford (1971).

32. W. Hauser and H. Feshbach, Phys. Rev. 87 366 (1952).

33. P. A. Moldauer, Nucl. Phys. A344 185 (1980).

34. A. Gilbert and A. Cameron, Can. J. Phys. 43 1446 (1965).

35. ABAREX, A Spherical Optical-Model Code, P. A. Moldauer, priv. com. (1982).

36. A. B. Smith, P. T. Guenther and R. D. Lawson, Nucl. Phys. A519 487 (1990).

37. A. B. Smith, P. T. Guenther and R. D. Lawson, Nucl. Phys. A483 50 (1988).

38. J. D. Jeukenne, A. Lejeune and C. Mahaux, Phys. Rev. C16 80 1970).

39. R. D. Lawson, A. B. Smith and S. Sugimoto, Bull. Am. Phys. Soc. 32 No.-1 32 (1987).

40. P. A. Moldauer, Nucl. Phys. 47 65 (1963).

41. R. L. Walter and P. P. Guss, Proc. Conf. on Nucl. Data for Basic and Applied Science, Vol.-2, p.-1079, Editors, P. Young, R. Brown, G. Auchampaugh, P. Lisowski and L. Stewart, Gordon and Breach, New York (1986).

42. G. R. Satchler Direct Nuclear Reactions Clarendon Press, Oxford (1983).

43. S. Chiba, R. Lawson, P. Guenther, M. Sugimoto and A. Smith, Argonne National Laboratory Report, ANL/NDM-119 (1991).

44. C. H. Johnson, D. J. Horen and C. Mahaux, Phys. Rev. C36 2252 (1987).

45. ANLECIS, A Coupled-Channels Code. A modification of the ECIS code of J. Raynal by P. A. Moldauer (1982).

46. S. Raman, C. H. Malarkey, W. T. Milner, C. W. Nestor Jr., and P. H. Stelson, Atom. Data and Nucl. Data Tables, 36 1 (1987).

47. S. F. Eccles, H. F. Lutz and V. A. Madsen, Phys. Rev. 141 1959 (1966).

48. S. Chiba, P. T. Guenther, R. D. Lawson and A. B. Smith, Phys. Rev. C42 2487 (1990).

49. Ch. Lagrange, NEA Report, NEANDC-228 (1982).

50. D. Madland and P. Young, Proc. Inter. Conf. on Neut. Phys. and Nucl. Data for Reactors and other Applied Purposes, Harwell (1978), OECD Press Paris.

51. D. Wilmore and P. E. Hodgson, Nucl. Phys. 55 673 (1964).

52. J. Rapaport, V. Kulkarni and R. W. Finlay, Nucl. Phys. A330 15 (1979).

53. J. P. Delaroche, Y. Wang and J. Rapaport, Phys. Rev. C39 391 (1989).

54. G. W. Greenlees, W. Makofske and G. J. Pyle, Phys. Rev. C1 1145 (1970).

55. C. J. Batty, E. Friedman and G. W. Greenlees, Nucl. Phys. A1127 368 (1969).

56. R. D. Lawson, P. T. Guenther and A. B. Smith, Phys. Rev. C34 1599 (1986).

57. A. B. Smith, P. T. Guenther and R. D. Lawson, Nucl. Phys. A455 344 (1986).

58. R. D. Lawson, P. T. Guenther and A. B. Smith, Nucl. Phys. A493 267 (1989).

59. A. B. Smith, P. T. Guenther and J. F. Whalen, Nucl. Phys. A415 1 (1984).

60. C. Johnson, A. Galonsky and R. Kernell, Phys. Rev. C20 2052 (1979).

61. R. D. Lawson and A. B. Smith, to be published.